frontiers | Frontiers in Astronomy and Space Sciences

TYPE Original Research
PUBLISHED 25 February 2025
DOI 10.3389/fspas.2025.1503042

Check for updates

OPEN ACCESS

EDITED BY
Jennifer Claire Stern,
National Aeronautics and Space Administration, United States

REVIEWED BY
Francesco Dela Pierre,
University of Turin, Italy
Ziqin Ni,
Georgia Institute of Technology, United States

*CORRESPONDENCE
Youcef Sellam,
youcef.sellam@unibe.ch

RECEIVED 27 September 2024
ACCEPTED 08 January 2025
PUBLISHED 25 February 2025

CITATION
Sellam Y, Gruchola S, Tulej M, Keresztes Schmidt P, Riedo A, Meddane S and Wurz P (2025) The search for ancient life on Mars using morphological and mass spectrometric analysis: an analog study in detecting microfossils in Messinian gypsum. *Front. Astron. Space Sci.* 12:1503042. doi: 10.3389/fspas.2025.1503042

COPYRIGHT
© 2025 Sellam, Gruchola, Tulej, Keresztes Schmidt, Riedo, Meddane and Wurz. This is an open-access article distributed under the terms of the Creative Commons Attribution License (CC BY). The use, distribution or reproduction in other forums is permitted, provided the original author(s) and the copyright owner(s) are credited and that the original publication in this journal is cited, in accordance with accepted academic practice. No use, distribution or reproduction is permitted which does not comply with these terms.

The search for ancient life on Mars using morphological and mass spectrometric analysis: an analog study in detecting microfossils in Messinian gypsum

Youcef Sellam[1]*, Salome Gruchola[1], Marek Tulej[1], Peter Keresztes Schmidt[1], Andreas Riedo[1,2], Sofiane Meddane[3] and Peter Wurz[1,2]

[1]Space Research and Planetary Sciences, Physics Institute, University of Bern, Bern, Switzerland, [2]NCCR PlanetS, University Bern, Bern, Switzerland, [3]Laboratory of Metallogeny and Magmatism of Algeria, Department of Geology, University of Science and Technology Houari Boumediene, Algiers, Algeria

Hydrated sulfate deposits have been detected on Mars. A spaceflight instrument capable of detecting microfossils in these salt deposits is highly important for the search for ancient life on Mars. This study employed a range of analytical methods, including nondestructive optical microscopy and SEM-EDX, as well as spatially resolved laser ablation mass spectrometry (LIMS), the latter being designed for in-situ analyses on planetary surfaces, to comprehensively examine the morphology, texture, mineralogy, and geochemistry of fossil-bearing gypsum deposits from Algeria. These extensive gypsum formations formed during the Messinian Salinity Crisis (MSC) and serve as excellent astrobiological analogs for the large-scale hydrated sulfate deposits detected on Mars. Significant research on Messinian gypsum reveals notable microbial fossil filaments. This study aims to determine whether optical microscopy and LIMS measurements together can detect fossil filaments in the gypsum samples, identify their composition, and decipher their biogenicity and syngeneity. Spatially resolved depth profiling and chemical mapping analysis of one representative fossil filament using LIMS provided detailed mineralogical and compositional variations that correlate with distinctive morphological features. These findings collectively indicate that the fossil filament exhibits distinct composition and diagenetic processes in comparison to the surrounding gypsum host. The microfossil's syngeneity and biogenicity were established based on the presence of morphological biosignatures, biologically relevant elements, and biologically induced or influenced minerals such as dolomite and clay minerals. The formation of these minerals within the physico-chemical context of ancient Martian lakes was also discussed. The same suite of measurements and techniques could be applied to study microfossil-bearing gypsum formations on Mars and beyond.

KEYWORDS

microfossil biosignatures, Messinian gypsum, martian surface, laser ablation ionization mass spectrometry, astrobiology, in-situ detection, space exploration

1 Introduction

Many astrobiological missions have been devoted to the exploration of various celestial bodies. Most of these missions have targeted the planet Mars with the primary objective being the search for evidence of extraterrestrial life (Enya et al., 2022b; De Mol, 2023b; Westall et al., 2015; Clark et al., 2021). These missions provided insights into e.g., the characteristics of the Martian geology and its paleoenvironment, suggesting the occurrence of past aqueous processes on Mars, including both subsurface and surface water (Squyres and Knoll, 2005; Carr and Head, 2003). The water activity on the surface of Mars, billions of years ago, led to the precipitation of sulfate minerals such as the mono-hydrated kieserite ($MgSO_4{\cdot}H_2O$), hemi-hydrated bassanite ($CaSO_4{\cdot}0.5H_2O$), anhydrite ($CaSO_4$), poly-hydrated minerals (such as, Mg-, Ca-, Na-, or Fe- $SO_4{\cdot}nH_2O$) and gypsum ($CaSO_4{\cdot}2H_2O$) (Gendrin et al., 2005; Clark et al., 2005; Vaniman et al., 2018; King and McLennan, 2010; Langevin et al., 2005).

Gypsum has been widely identified across the Martian surface (Bibring et al., 2005; Das et al., 2021). Two modes of gypsum formation on the Martian surface have been suggested; 1) Primary formation through volcanic fumarole vapor-deposition and chemical precipitation process (evaporites), and 2) secondary mineralization through hydration/dehydration and diagenesis of prior minerals by fluid/rock interactions (Hazen et al., 2023). Gypsum on Mars has been detected in a large dune field in Olimpia Planum (Massé et al., 2010), in Iani Chaos (Sefton-Nash et al., 2012), in Mawrth Vallis (Wray et al., 2010), in the Columbus crater (Wray et al., 2011), as veins in Endeavour Crater in the Cape York area (Squyres et al., 2012), and in Gale crater (Grotzinger et al., 2013; Ettehadi et al., 2023). In certain locations, such as Juventae Chasma and Mikumi crater, northern Meridiani Planum, sulfate deposit sequences were also detected (Baschetti et al., 2024; Catling et al., 2006). The chemistry of sulfates on Mars, indicative of ancient fluid interaction with alkali-basaltic rocks and/or regolith, combined with the thermodynamic constraints of gypsum formation–occurring only at low temperatures (~60°C in dilute fluids and below ~20°C in NaCl saturated brines) – and the presence of large scale layered patterns strongly supports a sedimentary origin for gypsum resulting from evaporation of a supersaturated standing body of water, rather than a volcanic body of water (Sgavetti et al., 2009b; Catling et al., 2006).

Apart from serving as a direct indication of the past aqueous environment on Mars and a useful proxy for decoding its paleoenvironment, the geochemistry of water on Mars could have supported microbial life and its potential preservation, similar to the early Earth, where life emerged about 4 billion years ago (Anderson et al., 2017; Yoshimura, 2019). Due to gypsum's fast growth allowing for the rapid entombment of cells, it exhibits exceptional fossilization potential and biosignature preservation (Natalicchio et al., 2022). Furthermore, gypsum's early formation in different geological systems (Benison and Karmanocky, 2014; Warren, 2016; Lugli et al., 2010) and its stability when exposed to present-day simulated Martian surface conditions further substantiates gypsum's potential as a significant target in the search for evidence of past life on Mars (Schopf et al., 2012; Natalicchio et al., 2022; Dela Pierre et al., 2015; Cloutis et al., 2007).

A substantial number of terrestrial analogs have been proposed to enhance our understanding of the geology, environmental dynamics, and astrobiological potential of sulfate minerals and hydrated gypsum deposits on Mars (Fernández-Remolar et al., 2005; Chan et al., 2004; Gaboyer et al., 2017; Benison and LaClair, 2003; Benison and Bowen, 2006). Among these, the Mediterranean Messinian evaporites are particularly noteworthy as they record the transition from positive to negative hydrologic budget conditions in the Mediterranean Sea during the so-called Messinian Salinity Crisis (MSC) (5.97–5.33 Ma) (Hsü et al., 1973; Sgavetti et al., 2009b; Barker and Bhattacharya, 2018; Krijgsman et al., 1991). The MSC involved the partial to complete isolation of the Mediterranean Sea from the Atlantic Ocean, likely driven by glacio-eustatic or tectonic processes (Krijgsman et al., 2024). During the MSC, a substantial volume of the Mediterranean Sea's evaporated, resulting in an increase in its salinity above contemporary levels and transforming it into a large hypersaline depositional environment (Schopf et al., 2012; Roveri et al., 2014). During its initial phase (5.97–5.60 Ma ago), 16/17 lithological cycles consisting of the alternation of thick bottom-grown gypsum beds and thin layers of organic-rich shales were deposited in marginal Mediterranean basins less than 200 m deep, forming the Primary Lower Gypsum unit (PLG), which reached up to 300 m in thickness (Lugli et al., 2010). These deposits are suggested as terrestrial analogs for some of the observed sulfate and clay alternations on Mars, including those in Arabia Terra, Meridiani Planum, and Juventae Chasma. These Martian deposits may have formed through desiccation of oceans or standing bodies of water during the Noachian era, as the planet transitioned from a wet to a dry state (Barker and Bhattacharya, 2018; Sgavetti et al., 2009b; Baschetti et al., 2024; Catling et al., 2006).

The extreme conditions of the MSC led to the extermination of most eukaryotic life thriving in the Mediterranean Sea (Bellanca et al., 2001). Consequently, only the fossils of a limited number of extremophile prokaryotes might have been preserved in Messinian gypsum (Allwood et al., 2013b). However, it was pointed out that the fossils of eukaryotes, such as diatoms, can be very abundant and extremely well preserved suggesting that gypsum does not necessarily reflect very shallow and hypersaline depositional conditions (Pellegrino et al., 2021). The PLG preserves both morphological and chemical evidence of prokaryotic communities, such as fossil filaments that were trapped during its formation (Oliveri et al., 2009; Dela Pierre et al., 2012; Dela Pierre et al., 2014; Dela Pierre et al., 2015; Schopf et al., 2012; Perri et al., 2017; Guibourdenche et al., 2022). The origin of the PLG fossil filament has been proposed to be benthic algae (Vai and Lucchi, 1977) or cyanobacteria (Panieri et al., 2010). Recently, the fossil filaments from a PLG have been interpreted as fossils of giant ecophenes colorless sulfide-oxidizing bacteria similar to modern *Beggiatoa* and *Thioploca*, based on similarities in size and the presence of small pyrite aggregates and associated polysulphides (Schulz and Jørgensen, 2001; McMahon et al., 2021; Oehler and Cady, 2014; Oliveri et al., 2009; Dela Pierre et al., 2012; Dela Pierre et al., 2014; Dela Pierre et al., 2015; Schopf et al., 2012; Perri et al., 2017; Teske and Nelson, 2006).

Prokaryotic communities are often found dwelling within modern evaporites, such as gypsum, forming in sabkhas, lacustrine, and marine terrestrial sediments. They mainly participate in carbon, iron, sulfur, and phosphate biogeochemical cycles, extracting water

and using various survival strategies to avoid ecological stresses (Sajjad et al., 2022; Huang et al., 2020; Teske and Nelson, 2006). Consequently, investigating these fossil filaments may enhance our comprehension of the cryptic conditions that led to the formation of the PLG during the MSC, the biosignature preservation potential of gypsum, and the possible preservation of such fossils in ancient, hydrated sulfate deposits on Mars.

In this study, we investigated the morphology, elemental composition, and mineralogy of a fossil filament preserved within primary bottom-grown gypsum selenite formed during the MSC in the Chelif marginal basin, Algeria. Optical microscopy, Scanning Electron Microscopy (SEM), Energy dispersive X-ray analysis (EDX), and Laser Ablation Ionization Mass Spectrometry (LIMS) were employed to assess the biogenicity and syngeneity of the fossil filament, highlighting its relevance to the search for past life in Martian hydrated gypsum and sulfate deposits.

2 Materials and methods

2.1 Geological settings and sample description

The studied gypsum was sampled from the Sidi Boutbal quarry (SB), (35°42′36.5″N 0°21′57.4″W), located in the Oran district, Algeria. This quarry is situated at the eastern extremity of the Lower Chelif basin (Mediterranean Basin) (Figure 1A). The Chelif Basin is one of the largest Messinian peripheral sub-basins, characterized by an elongated and ENE–WSW oriented structure spanning over 260 km in length and 35 km in width. It is situated between the sabkha of Oran to the west and El Asnam city to the east (Rouchy et al., 2007).

The SB quarry is predominantly composed of an Upper Miocene to Plio-Quaternary succession, exhibiting is an anticlinal structure that exposes a 60 m thick evaporitic succession at its core. This succession consists of bottom grown gypsum beds comprising of twinned selenite crystals. Four gypsum beds (Gb1, Gb2, Gb3, and Gb4), interbedded with thin clay and sandstone layers are recognized, as illustrated in Figures 1C–E. However, only the Gb2, Gb3, and Gb4 are visibly exposed in the outcrop. About 30 kg of gypsum, containing preserved filaments, were collected from the 15 m thick third gypsum bed (Gb3) using a hammer and chisel (asterisk symbol in Figures 1C–E). The sampled gypsum rock was subsequently packed in plastic bags for further preparation and to minimize contaminations. The gypsum rock exhibited a light gray to brown coloration, manifesting as either small crystal selenite (0.5 – 2 cm) (SC, Figure 2A) or 10 cm-sized twinned arrow-head selenite crystals (TS, Figure 2A). It displayed an alternation of millimeter-thick turbid and limpid laminae, visible by eye. The limpid laminae exhibited rare to absent visible solid inclusions, while the turbid laminae contained a concentrated network of up to millimeter-long brownish filaments within the re-entrant angle of the twinned selenite crystals (Figure 2B).

2.2 Sample handling

During sample preparation, measures were implemented to prevent contamination from the rock's surface and external sources. A hand-sized gypsum rock was meticulously cleaved to unveil a pristine, uncontaminated surface. A 1 mm in thick segment of gypsum was meticulously extracted from this surface using a sterilized spatula. No additional processing was conducted. An initial examination using optical microscopy was performed on several thin sections to select the most suitable one for the study presented here. A small fraction of the representative thin section (Figure 2B) was subsequently prepared for analysis with SEM and EDX (Department of Chemistry, Biochemistry and Pharmaceutical Sciences, University of Bern, Switzerland) and LIMS by fixing the thin section on a LIMS-specific sample holder using conductive copper tape (Figure 2C). Finally, the sample was gold sputter coated (~10 nm gold layer) to enhance the sample surface for both SEM and LIMS analyses (Figure 2D; Gruchola et al., 2022). Through the use of optical microscopy, SEM and EDX measurements, one well-preserved filament was identified and selected for the subsequent, detailed LIMS chemical analysis.

2.3 Laser Ablation Ionization Mass Spectrometry (LIMS)

A detailed description of the space-prototype LIMS instrument used in this study can be found in previous publications, such as (Grimaudo et al., 2020) and references therein. Only a brief overview of the mass spectrometric system and its principle of operation are given in the following.

The LIMS system consists of a miniature reflectron-type time-of-flight (R-TOF) mass spectrometer to which a laser ablation ion source is coupled. The latter is a pulsed femtosecond laser system, with a pulse repetition rate of 1 kHz, a pulse width of $\tau \sim 190$ fs, and emits a fundamental laser beam at wavelength of $\lambda = 775$ nm. This beam is then converted to 258 nm using a harmonic generator unit. The 258 nm output is further split into two laser beams of similar pulse energy, delayed by about 40 ps, and recombined collinearly in a double-pulse (DP) unit (Tulej et al., 2018; Riedo et al., 2021). Two laser beam attenuators allow the precise adjustment of both pulse energies before recombination. After the DP unit, a beam guiding system guides the laser beam through a beam expander, through the entrance window of the vacuum chamber and through the mass analyzer towards the sample surface. A 3D translation stage allows accurate positioning of the sample surface relative to the entrance electrode of the mass analyzer (Figure 3).

Each laser pulse ablates and ionizes a distinct layer from the sample material. The ion-optical system of the mass analyzer collects the positively charged ions and guides them towards the detection unit (MCP detector system). Note, in this study the signal was only collected from one of the four anodes (Riedo et al., 2017). Species arrive sequentially at the detector system according to their mass to charge ratios (m/q). The TOF signal is recorded with a sampling speed of 3.2 GS/s using a high-speed ADC data acquisition system. For the automation and control of the entire instrument (laser system, data acquisition, sample stage, and pulse delay stage), in-house written software is used.

In all measurement campaigns, the applied voltage difference over the MCPs in the detector unit was set to 1700 V. LIMS measurements on the gypsum sample were conducted using pulse

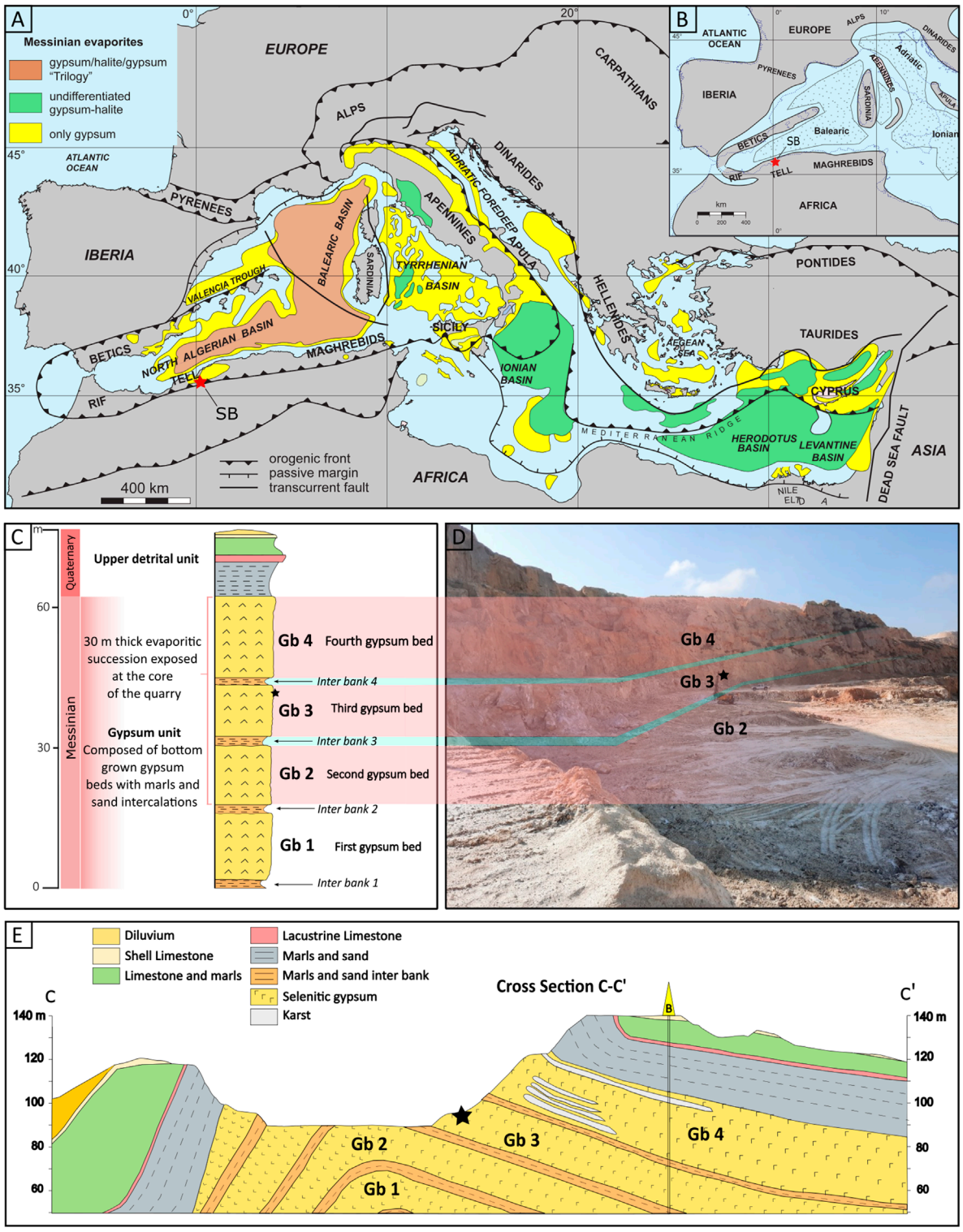

FIGURE 1
Geographical and Geological context. **(A)** Map of the Mediterranean Sea showing the evaporites distribution (modified after Manzi et al., 2012). **(B)** Paleogeographic map of the Western Mediterranean during the Messinian salinity crisis, highlighting the principal evaporite depocenters with dotted areas (modified after Manzi et al., 2012). Emerged regions are shaded in gray, while a dotted line denotes the modern coastline. The asterisk designates the study area; Sidi Boutbal quarry, Lower Chelif basin, Algeria. **(C)** Schematic stratigraphy of the SB quarry. **(D)** The boundary between the gypsum bed 4, 3 and 2. **(D)** Geological cross section of the Messinian deposits of the Sidi Boutbal quarry. The red asterisks in **(A, B)** indicates the Sidi Boutbal quarry location and the black asterisks in **(C, D, E)** indicate the sampled gypsum bed unit 3.

10.3389/fspas.2025.1503042

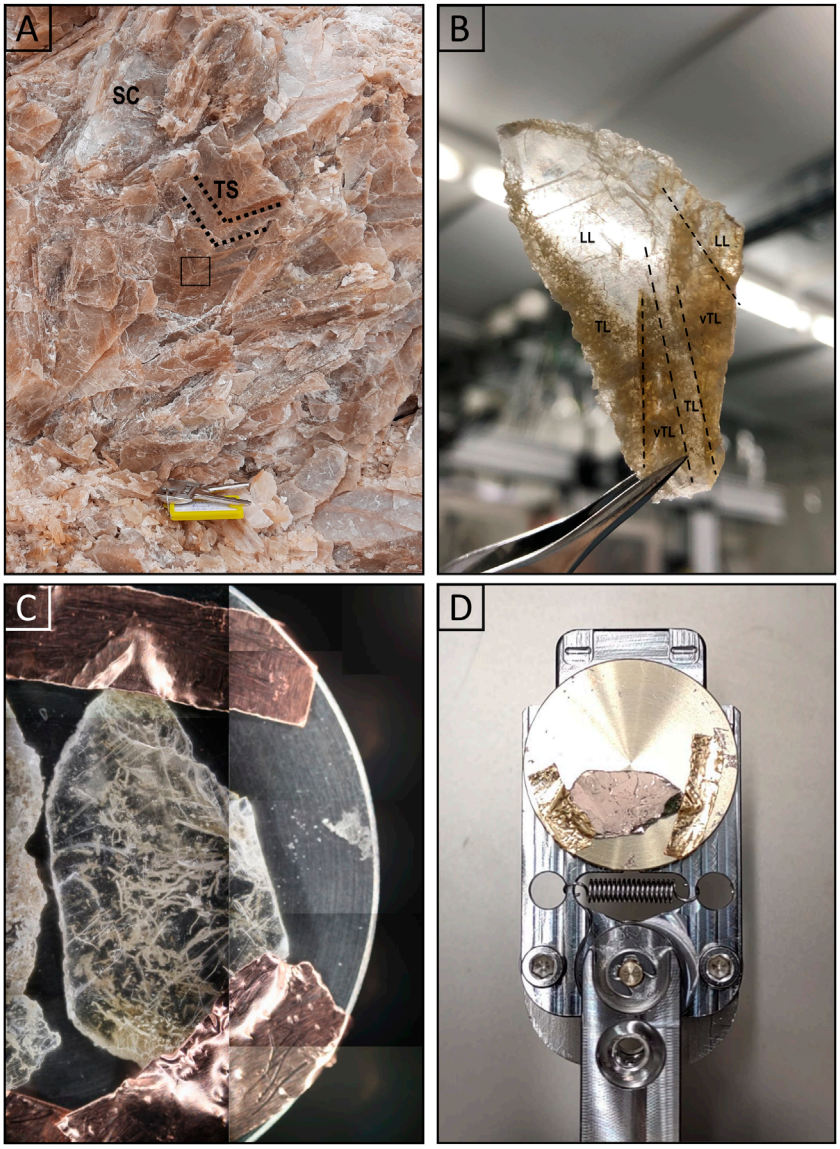

FIGURE 2
Gypsum's crystalline facies and sample handling. Images of the studied twinned selenite crystal and of the sample preparation and handling for optical microscopy, SEM-EDX, and LIMS analyses. **(A)** Smal crystal selenite (SC) and decimeter-sized twinned arrow-head selenite (TS) crystals show the darker re-entrant angle of the crystals (dashed black lines). **(B)** Large petrographic thin section of the re-entrant angle of the twinned selenite crystal marked in the blue rectangle in **(A)**. It shows very turbid (vTL), turbid (TL) and limpid laminations (LL). **(C)** Small petrographic thin section of turbid laminae fixed on the LIMS sample holder with copper tape. **(D)** Gold coated sample on the LIMS sample holder.

energies of 3.0 μJ and 3.2 μJ with a pulse energy stability of about ±0.1 μJ for the first and second pulse, respectively. These values refer to pulse energies measured at the laser focus on the sample surface. LIMS measurements covering both gypsum and the selected fossil filament regions (Figure 4) were conducted in a grid of 17 × 25 spots (Figures 5A,C), (the data used for the sample analysis covered an area of 11 × 12 craters (Figure 5D)).

In this measurement, 800 laser bursts were applied to each sampled location. Each burst consisted of 50 laser shots, for a total of 40,000 laser shots per sample. For each burst, the mass spectra of the individual laser shots were histogrammed into a single spectrum. This allows the analysis of the chemical composition of the ablated layers with a resolution at the μm level and lower. Subsequent to data collection, 2D atomic fraction maps were produced for the analyzed area. Depth profile analyses were conducted for the individual locations to understand the spatial heterogeneity of the sample at the μm spatial scale. Through element intensity correlations, the mineralogical composition of the sample can be derived. Atomic Force Microscopy (AFM) measurements were performed to correlate between the number of laser shots and crater depth, allowing for an accurate inclusion size measurement. The description and the results of the AFM measurements are summarized in the supplementary material section.

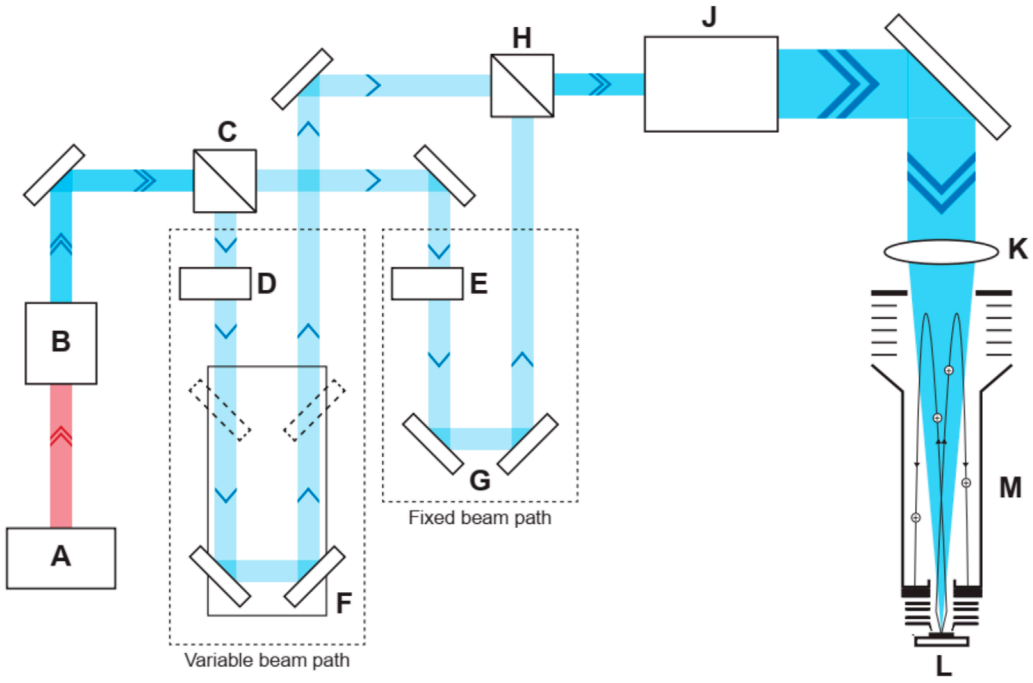

FIGURE 3
Schematic overview of the double pulse laser system. Schematic overview of the double pulse laser system and mass analyzer. **(A)** Laser system that provides a pulsed laser beam (λ = 775 nm, τ = 190 fs, rep. rate = 1 kHz, P = 1 W). **(B)** Harmonic generator unit that provide a laser beam (λ = 258 nm, P = 140 mW) after conversion. **(C)** First beam splitter. **(D)** Motorized attenuator for the first beam. **(F)** Retroreflector mounted on a linear translation stage. Variations in time delay between the two laser beams are controlled by the position of the retroreflector. **(E)** Second motorized attenuator for the second beam. **(G)** Fixed retroreflector for the second beam. **(H)** Second beam splitter to recombine the two laser beams. **(I)** Beam expander. **(J)** Doublet lens. **(L)** Mass analyzer. **(K)** Sample.

3 Results

3.1 Optical microscopy and SEM and EDX analysis

Optical microscopy analysis of the SB Gb3 sample under transmitted plane-polarized light showed that turbid laminae consist of a densely interwoven network (Figure 4A) of brownish, sinuous, and curved fossil filaments (Figure 4B) of various sizes (ranging from μm to mm length and 20–80 μm width) (Figure 4A, white triangles). Under reflected plane-polarized light, the fossil filaments appear to be partially hollow (arrows in Figure 4C) and exhibit different mineralogical compositions (Figures 4C,E,F). The fossil filaments are syngenetic and embedded within gypsum, as they are situated on the side opposite the focal plane of a secondary veinlet (arrows in Figures 4B,E,F). Close observation of the fossil filament under transmitted cross-polarized light reveals the presence of spherical to subspherical grains measuring 5–10 μm in size, typically with sharp edges, high relief, and high birefringence (Figures 4D,J). Additionally, within the filament, scattered opaque black grains of varying sizes are present (arrows in Figure 4K), while the area surrounding the fossil filament appears dark. Fluid inclusions, mainly rectangular in shape, were observed in all the examined thin sections. A close-up SEM analysis of a hollow fossil filament (~80 μm width) revealed an inner layer (~15 μm) composed of two main minerals (Figure 4G). The predominant mineral is formed by spherical to subspherical crystals, often hollow (~5–10 μm), with EDX spectra indicating the presence of C, Mg, Ca, and traces of Si, corresponding to Mg-Ca carbonate minerals (Figure 4I, red spectrum). These crystals are intercalated by a flaky, wavy subhedral thin to thick layered aluminosilicate mineral (clay minerals) composed of C, O, Mg, Al, Si, Fe, and traces of K (EDX spectra, Figure 4I, blue spectrum). The inner layer of the filament is morphologically and compositionally distinct from the gypsum, mainly composed of Ca, S, O, and traces of Si (Figure 4I, yellow spectrum).

3.2 LIMS

The area selected for LIMS measurements was sampled at 425 single surface positions (Figures 5B,C). The abundance of elements related to gypsum (O, S, Ca) and the fossil filament were analyzed in detail for the 425 positions (Figure 6). The gypsum element intensities are uniformly distributed across the sampled area, except in or around the filament. There, O, S, and Ca intensities drop significantly (Figure 6A, rows 2–7). Al, Si, C, and Mg intensities are at the background signal level (Figure 6A, middle and bottom panels). However, a significant increase in their intensities is observed in and around the filament (rows 2–10), with the presence of noticeable double peaks in rows 3–9 that align with the filament edges and decrease in intensity that corresponds to the hollow area (Figure 5D, rows 3–9). This pattern is evident as the measurement's direction intersects the fossil filament (see black

10.3389/fspas.2025.1503042

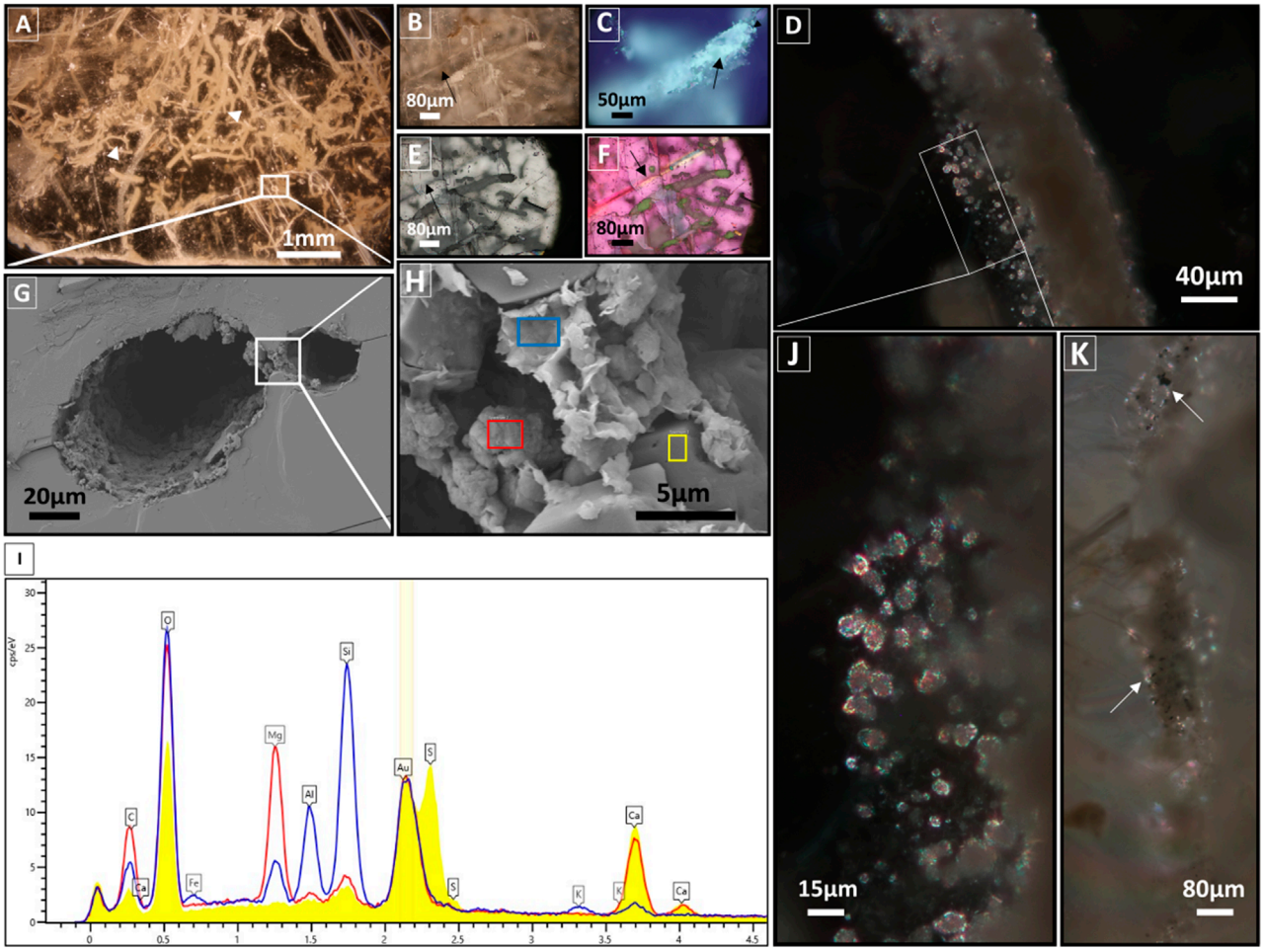

FIGURE 4
Optical microscopy and SEM images and EDX spectra. Optical microscopy images, under transmitted plane-polarized light **(A, B)**, reflected plane-polarized light **(C, E, F)**, transmitted cross-polarized light **(D, J, K)**. SEM images **(G, H)** and SEM-EDX spectrum **(I)** of permineralized filamentous microfossils within the turbid laminae. **(A)** Network of sinuous µm long filaments to mm long curved fossil filaments (white triangles), and 20–80 µm width. **(B)** Close-up image of fossil filament with two exposed sides showing the filament's position to the crystal plane. **(C)** Image of hollow to partially hollow filament (black arrow). **(E, F)** Images show the offset of the gypsum-embedded fossil filament, contrasting with a secondary veinlet (black arrows). **(D, J)** Images showing high birefringence of the subspherical minerals. **(K)** Image of a fossil filament with black and opaque inclusions (white arrows). **(G)** SEM image of hollow filament marked in **(A)**. Note the presence of an attached small hole on the right side of the fossil filament. **(H)** Magnification of the marked white rectangle in **(G)** showing the different mineral located in the inner layer of the hollow filament. **(I)** Comparison of EDX spectra of the fossil filament (blue and red) with the host EDX spectrum (yellow) (measured locations are indicated in **(H)**). (the three spectra were normalized to the ^{197}Au cps/eV value).

arrows in Figure 5C). The chemical composition difference is further illustrated in Figure 6B, where the intensity distribution of several elements across locations 91–101 are shown (Figure 6A row 2, see red rectangle in Figure 5D for location on the sample). At locations 92 to 99, corresponding to locations at and around the filament, the intensities of K, Li, Mg, Al, Si, C, B, and Cl increase significantly compared to gypsum locations 101 and 102, where only O, Na, Ca, and S were detected above the noise level, as expected for gypsum. A smaller increase is observed for P, F, V, Cr, Mn, and Co. Given the distance of 20 µm between single laser ablation craters, the length of the fossil filament in the horizontal direction is approximately 100 µm.

Figure 7 shows a comparison of mass spectra recorded from two distinct locations on the filament (location 110 and 144) and one location on gypsum (location 230) (Figure 7A). The mass spectrum of the filament at location 110 reveals the presence of numerous metallic and non-metallic minor elements, including Li, B, C, F, Al, P, S, Cl, K, Ti, V, Cr, Mn, Fe, Co., and Sr, alongside the major elements O, Mg, Si, and Ca. In contrast, the spectrum of the filament at location 144 (Figure 7B) exhibits distinct elemental abundances: F, Na, P, and Mg are less abundant, and significantly lower intensities are observed for Li, Al, and Si. Furthermore, B, F, Cl, V, Cr, Mn, Fe, and Co. are not detected at location 144. Consequently, the presence of these elements is correlated with the abundance of Al and Si, and similar relative abundances of these elements can be observed on average at each ablated location. A more pronounced variation in elemental abundance is evident when analyzing depth profiles, where micrometer-sized features (though

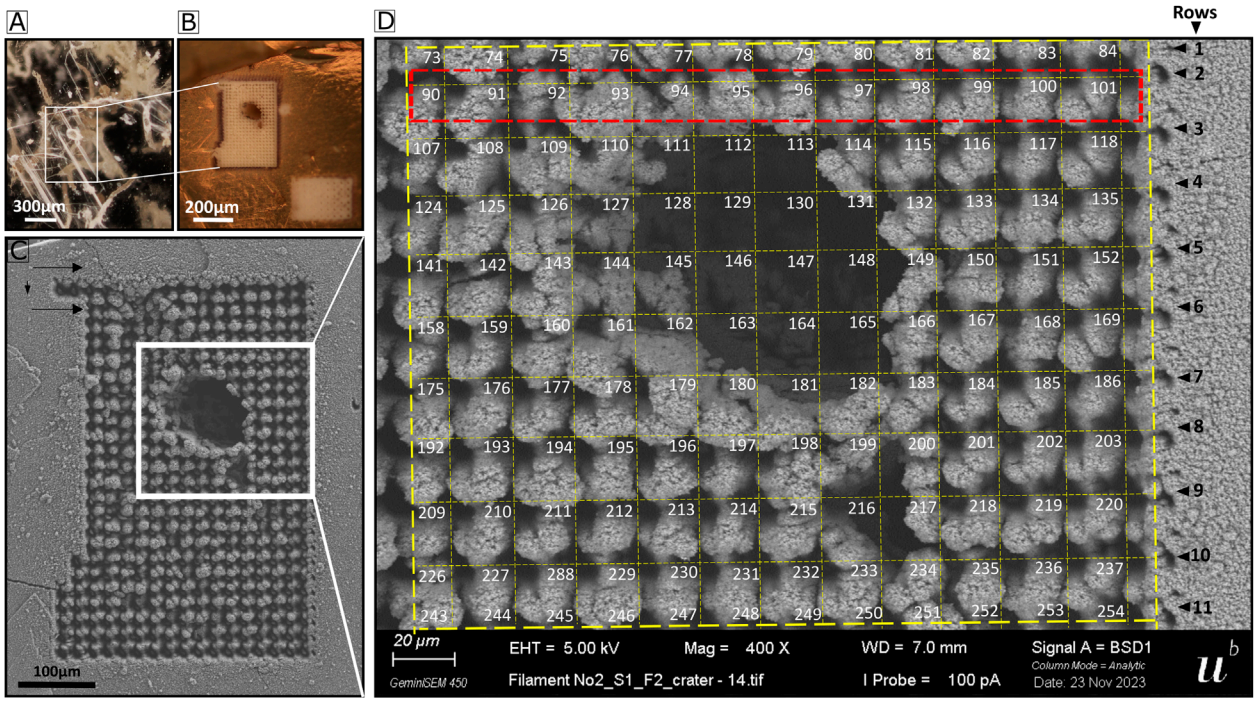

FIGURE 5
Sampled area and the grid of the analyzed area. **(A)** Optical image of the fossil filament. **(B)** Optical image of the filament after gold coating and LIMS campaign. **(C)** SEM image of laser ablation craters of the LIMS covering the fossil filament area, forming a grid of 17 × 25 craters. The direction of measurement is indicated with arrows. **(D)** SEM image of the area chosen for data analysis, forming a grid of 11 × 12 laser ablation craters.

less abundant) with varying elemental composition can be identified (e.g., carbonaceous deposits and other mineralogical grains like e.g., dolomite and clay minerals), as discussed below. The gypsum mass spectrum reveals the presence of H, O, S, Ca, and Na as major elements along with B, C, K, and Sr as minor trace elements, with concentrations at the ppm level. Some of the isotopes of Ti, Fe, Ni, Cu, Zn, As, and Se (Figure 7A) exhibit isobaric interference with several polyatomic species that correspond primarily to molecular species with compositions of $Ca_xS_yO_z$. It is noteworthy that an intensity increase for Ti is observed as well for its isotopes (^{46}Ti, ^{47}Ti, ^{49}Ti, ^{50}Ti), while an isobaric interference of ^{48}Ti with $^{32}S^{16}O$, and ^{50}Ti with $^{34}S^{16}O$ or $^{32}S^{18}O$ cannot be ruled out. Nevertheless, the observation of mass peaks from other isotopes confirms the presence of Ti. For the observation of ^{56}Fe (Figure 7A), the interference with $^{28}Si_2$, Al_2, and $^{40}Ca^{16}O$ cannot be ruled out. However, given that the $^{54}Fe/^{56}Fe$ isotope ratio is close to the expected value, the isobaric interferences appear to be minor.

The presence metallic and non-metallic elements at the filament location (Figure 7, location 110) C, H, N, O, P, S, Ca, Mg, Na, K, Cl, Al, Li, Cr, B, Si, F, V, Mn, and Co. can be attributed to two distinct groups 1) Biologically relevant elements, and/or 2) Elements involved in the mineral formation. This attribution is due to the faith of these elements before, during, and after the filament's fossilization process. The biologically relevant elements are chemical elements essential for living organisms' structure and function. The minerals within the fossil filament could have been controlled, induced, or influenced by the presence of living organisms or their organic matter. During the fossilization process, minerals that had been formed previously interact with the organic matter, resulting in its complete or partial replacement by a mineral phase. The elements within the organic matter could either be involved in the mineral formation, adsorbed, or preserved as organic inclusions. Thus, some detected elements within the fossil filament, such as C, H, O, Ca, Mg, Al, and Si, are attributed to both groups.

The biologically relevant elements C, H, N, O, P, and S (CHNOPS) constitute the bulk of major macromolecules. Ca, Mg, Na, K, and Cl are the major ions within procaryotic cells, while the main transition metals detected are V, Cr, Mn, and Co. The N peaks at m/z 14 show isobaric interference with Si^{++} and is excluded from further analysis. B, Si, and F are involved in specialized metabolic processes (Kabiraj et al., 2022; Wackett et al., 2004; Ikeda, 2021). Lastly, Al, Li, and Cr are reduced and/or methylated by some prokaryotes. These elements were not found in the host, except for H, O, S, and Ca, typical gypsum components. B, C, Na, and K can be attributed to fluid inclusions within gypsum. Sr was also detected at the gypsum location and its presence is due to a substitution with Ca in the lattice during gypsum formation (Fei et al., 2022). Fe, Ni, Cu, Zn, As, and Se are also biologically relevant elements, but because of potential isobaric interferences with polyatomic species, they will not be discussed further.

High intensities of elements including H, O, Na, Mg, Al, Si, Ca, and K, and the difference of composition in locations 110 and 144, suggest that the inner filament layer is likely composed of a mixture of mineralogical species. A grid of 11 × 12 positions (in total 132 positions) (Figure 5D) was selected for further analysis, and atomic fraction maps were generated for selected elements, categorized into

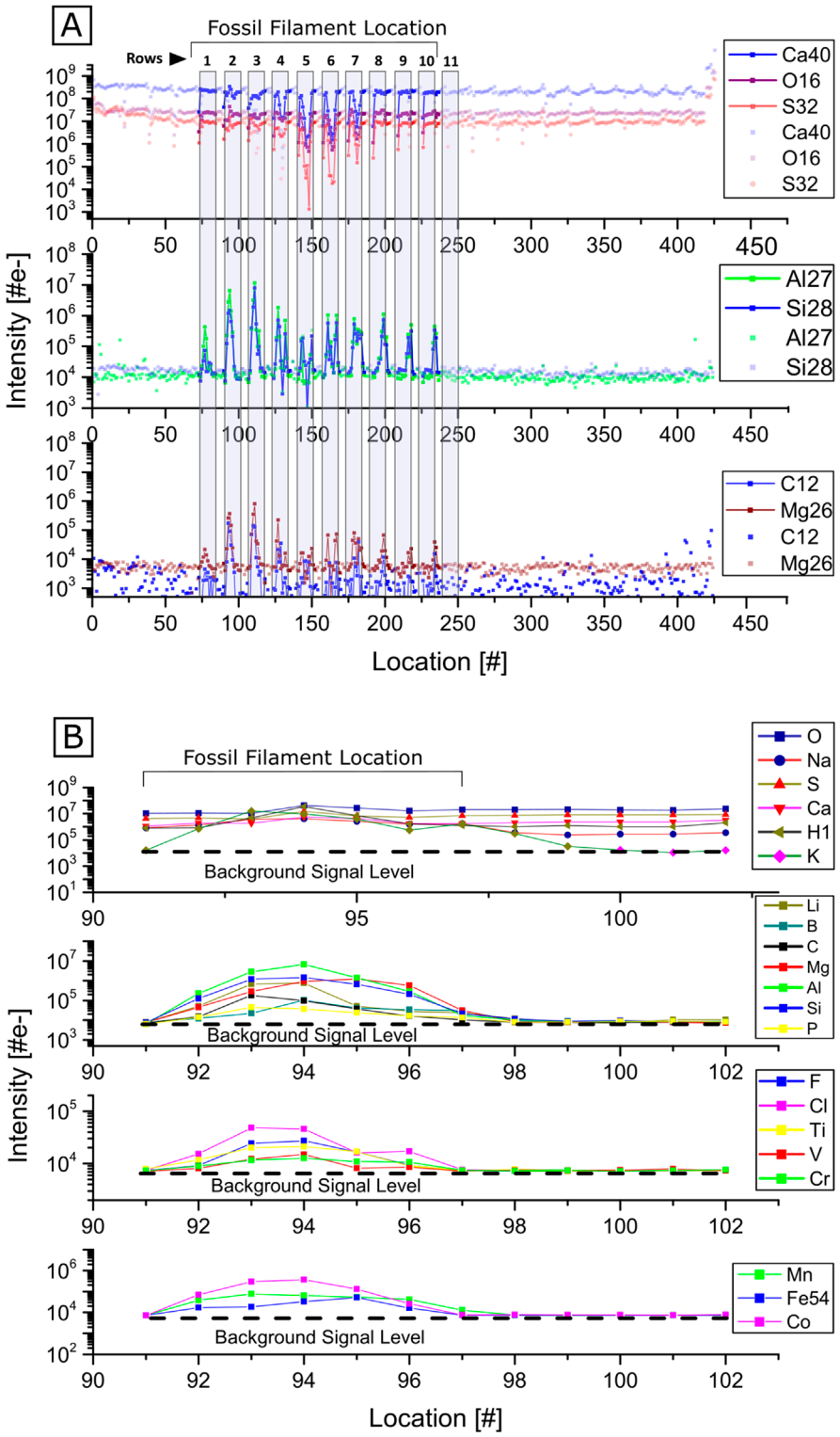

FIGURE 6
Element intensities at each location. **(A)** Element intensities at each location sampled with LIMS. An intensity decrease of O, S and Ca can be observed at locations near and on the fossil filament, while Li, Al, Si, C and Mg experience an intensity increase at locations associated with the fossil filament. **(B)** Detail of the intensity distribution for the crater locations 91–101. The filament location can be inferred from the intensity increase of various elements at the corresponding locations.

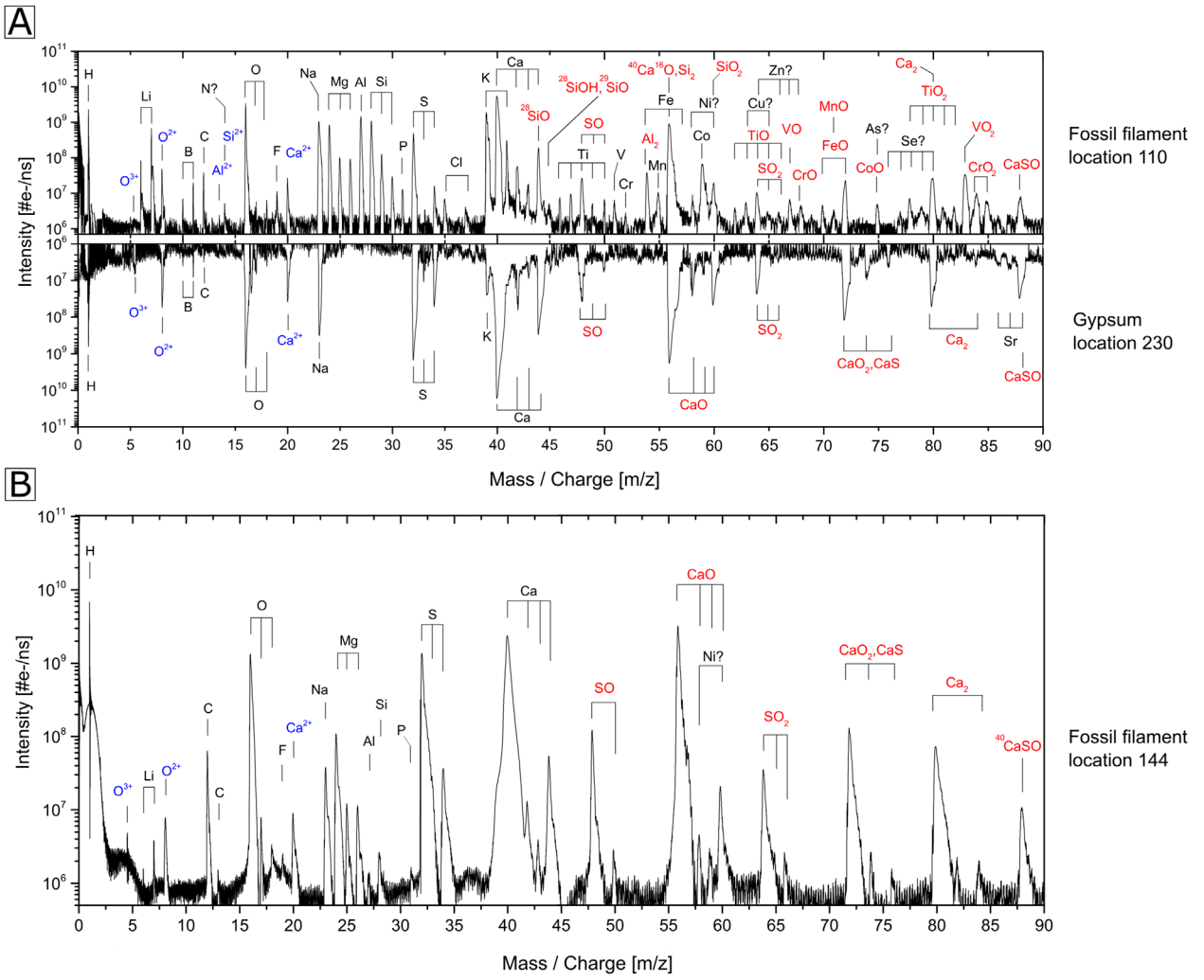

FIGURE 7
Comparison of spectra of fossil filament (location 110 and 144) with host. **(A)** Comparison of the mass spectra recorded at the fossil filament location 110 (upper trace) and gypsum (lower trace with inverted intensities). **(B)** Spectrum recorded at location 144 on the filament.

groups of biologically relevant elements and elements attributed to the mineral formation (Figure 8). For this analysis, the measured element intensities were corrected using relative sensitivity factors (RSCs) to obtain quantitative concentrations. The RSC factors were obtained from the mass spectrometric analysis of the geological standard reference material NIST SRM 610 and are summarized in the supplementary material section. The RSCs for H and B were assigned a value of 1 (no correction), as they are not certified within SRM 610. The same applies to C and F, but the RSC for C was assumed similar to Si and the RSC for F similar to Cl (similar physical and chemical properties). During the ablation and ionization process, some elements are easier to ionize (e.g., alkali elements) than others (e.g., F, Cl, O, S, C, Si). With the additional study of the SRM 610 geological standard, the determination of calibration factors to correct for the nonstoichiometric ionization efficiency becomes feasible (Neuland et al., 2016).

In Figure 8, the filament's position within the studied area is indicated by significant increases or decreases in the intensities of specific elements observed at the corresponding locations (refer to, for instance, the intensity maps of ^{27}Al and ^{28}Si). This indicates a mineralogical composition distinct from the host material. The CHNOPS elements (excluding N, as explained earlier) and elements pertinent to microbial building blocks and metabolism can be identified in both the filament core and its surrounding layer. The H and O content in gypsum ($CaSO_4 \cdot 2H_2O$) is notably lower compared to the fossil filament. The low H and O content is potentially attributed to the partial desiccation of gypsum to hemi-hydrate sulfate bassanite or the dehydrated anhydrite accruing in the vacuum chamber before LIMS measurements were started, although gypsum is considered quite stable at temperatures below 300 K (Tang et al., 2019). In contrast, the observed high H and O content within the fossil filament suggests the presence of hydrated swelling minerals and/or organic inclusions. In gypsum, S, Ca, and Na exhibit higher concentrations compared to the filament commensurate with the gypsum composition. The fossil filament is distinguished by a distinct composition evident by substantial enrichment of C,

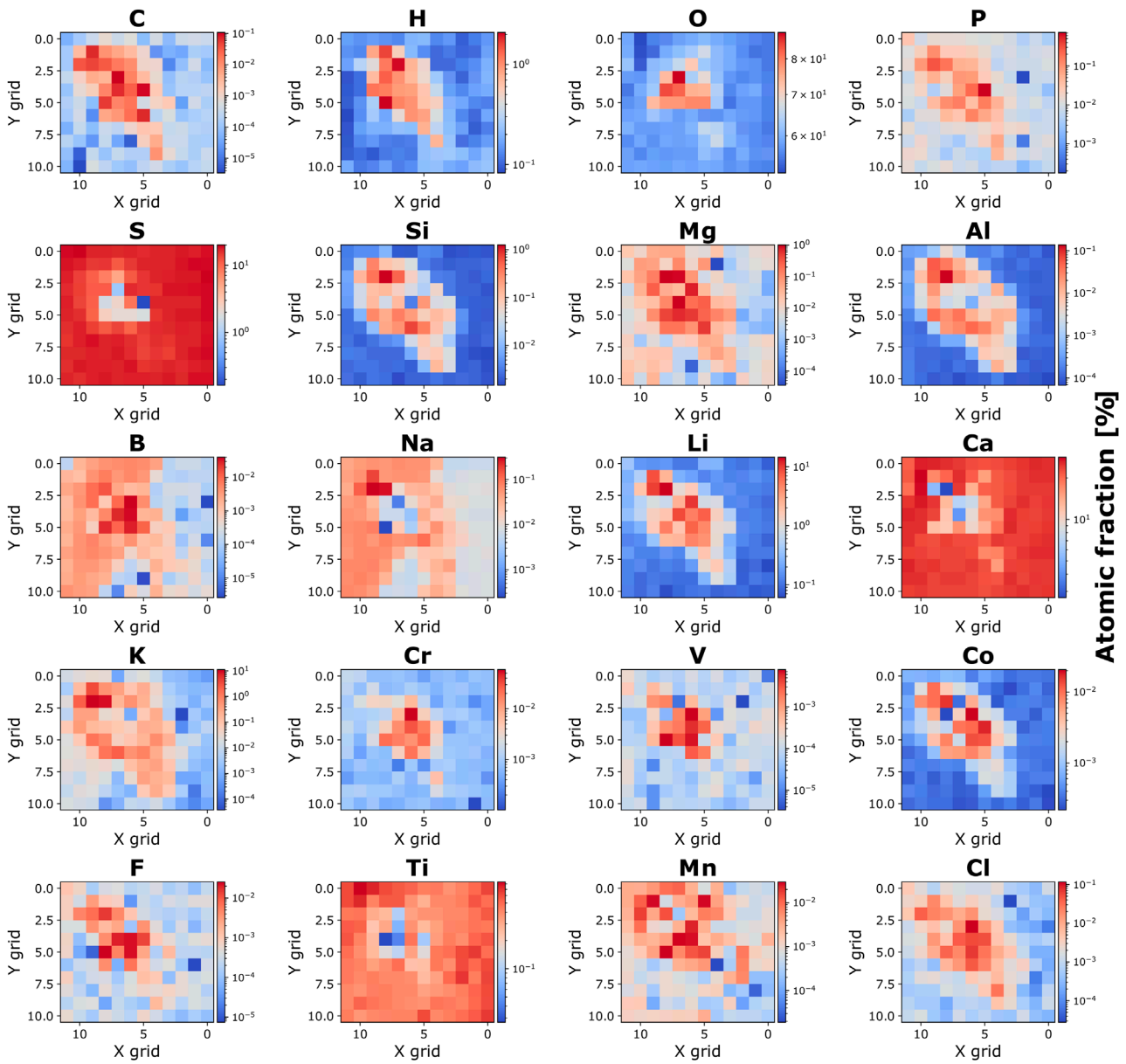

FIGURE 8
2D atomic fraction maps. 2D atomic fraction maps of the detected biologically relevant elements and elements involved in mineral formation. Nitrogen (N) is not shown due to potential isobaric interference with $^{28}Si^{++}$.

H, O, P, Mg, Al, Si, Li, K, Cr, V, Co., Mn, and Cl. This zone is of significance because it emphasizes the unique composition by presence of biologically relevant elements and mineralogical characteristics found in the inner layers of the fossil filament.

Figure 9A shows the chemical depth profile analysis of the gypsum mineral (location 90). There, the intensity of Ca, S, and O decays smoothly with increasing ablation layer, as expected for depth profile studies of a homogeneous composition (Grimaudo et al., 2020). The Si, Al, C, and Mg intensities show similar behavior and appear to be at background level over the 800 ablated layers. Figure 9B shows the chemical depth profile for the elements ^{12}C, ^{24}Mg, ^{27}Al, ^{28}Si, ^{40}Ca, ^{32}S, ^{16}O and H of the fossil filament (location 94) for the first 300 ablation layers. In the first 35 layers, an increase of the ^{12}C intensity is anti-correlating with a decrease in ^{24}Mg, ^{27}Al, ^{28}Si, ^{40}Ca, ^{16}O, and H intensities. At the ablation layers 35 to 50, a significant drop of the ^{12}C intensity is observed, and anti-correlated with a considerable intensity increase of ^{24}Mg, ^{27}Al, ^{28}Si, ^{40}Ca, and H. This is followed by a second intensity peak of ^{12}C and an intensity drop of ^{24}Mg, ^{27}Al, ^{28}Si, ^{40}Ca, and H at the ablation layers between 50 and 60, which anti-correlate again, indicating layers of carbonaceous deposits. At the ablation layers 110 to 140 and 190 to 210, two double peaks of ^{12}C and ^{24}Mg are perfectly correlating with a smooth increase of ^{40}Ca and ^{16}O at that depth. An interesting intensity drop of ^{32}S at the ablation layers from 170 to 210 anti-correlating with the second double peaks of ^{12}C and ^{24}Mg, and the smooth increase of ^{40}Ca and ^{16}O, suggests

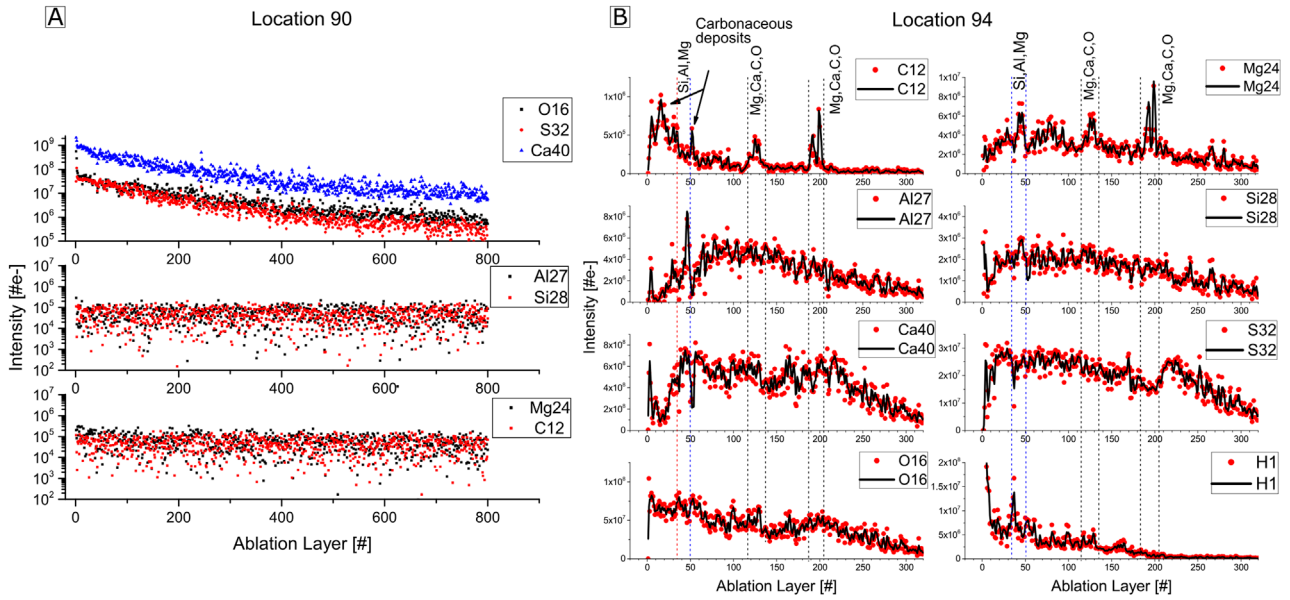

FIGURE 9
Chemical depth profiles. **(A)** Chemical depth profiles over 800 ablation layers for the isotopes ^{16}O, ^{32}S, ^{40}Ca, ^{27}Al, ^{28}Si, ^{24}Mg, and ^{12}C, at location 90 corresponding to gypsum. **(B)** Chemical depth profiles over 300 ablation layers for ^{12}C, ^{24}Mg, ^{27}Al, ^{28}Si, ^{40}Ca, ^{32}S, ^{16}O, and ^{1}H, at location 94 on the fossil filament.

an inclusion of a mineral formed from Mg, Ca, C and O. Based on the AFM results, the size of the Mg, Ca, C, and O forming mineral, spanning 10 to 15 ablation layers, can be estimated to be approximately 8–10 μm in thickness. This measurement correlates with the size and mineralogical composition of the subspherical mineral observed in Figure 4.

4 Discussion

4.1 Mineralogy and chemical composition of the fossil filament

As can be observed by eye and optical microscopy in Figures 2C, 4A–E, the Algerian PLG is characterized by long, hollow, sinuous, interwoven, pristine fossil filaments embedded in gypsum. Similar filamentous structures were documented in the PLG units at various locations across the Mediterranean Basin such as Italy (Panieri et al., 2010; Dela Pierre et al., 2015; Guibourdenche et al., 2022; Schopf et al., 2012), Spain, Greece (Natalicchio et al., 2022) and Cyprus (Allwood et al., 2013b).

The LIMS results enable the localization and investigation of the fossil filament's chemical composition (Figures 6, 7), which reveals a complex and distinguished mineralogical composition from the host. The high intensity of the major elements at the edges of the filament and the significant intensity decrease in the middle (Figure 6A) are due to the hollowness of the filament, as observed under optical microscopy and confirmed with SEM (Figures 4F,G).

Considering the shape, color, and optical mineralogy of the different minerals observed within the filament (Figure 4) along with the LIMS results, the dominant mineralogical species are 1) Dolomite, 2) Clay minerals, and 3) Pyrite. Dolomite (CaMg $(CO_3)_2$), include its precursor phases such as high-magnesium calcite ((Ca,Mg) CO_3), disordered dolomite, and protodolomite (Fang et al., 2021), which exhibits variable Mg and Ca ratios across different locations in the filament. Calcium carbonates ($CaCO_3$) and magnesium carbonates ($MgCO_3$) might also be present but in minor concentrations. Clay minerals are identified by the heightened intensities of Si, Al, O, and H (Figure 7A), which are key components of the basic framework of clay minerals. Pyrite observed as black, opaque framboidal grains of rare and scattered occurrence (Figure 4K). The detailed analysis of pyrites using LIMS would require a specialized measurement campaign (Lukmanov et al., 2022), which is beyond the scope of this study.

Dolomite may exhibit different Mg/Ca ratios in distinct crystals within the measured spot and between the different locations, accounting for the stoichiometry variability, as depicted in the atomic fraction maps in Figure 8 across the filament. Additionally, the composition of clay minerals is diverse, potentially incorporating additional elements present in the depositional environment (Brigatti et al., 2006).

Clay minerals are composed of cations coordinated with oxygen atoms. Common cations include Si^{4+}, Al^{3+}, Fe^{3+}, and Mg^{2+}, but other cations, such as Li^{+}, Mn^{2+}, Co^{2+}, Ni^{2+}, Cu^{2+}, Zn^{2+}, V^{3+}, Cr^{3+}, and Ti^{4+} have also been detected within clay minerals (Brigatti et al., 2006). Cation exchange in clay minerals is reversible, diffusion-controlled, stoichiometric, and often selective for one cation over another (Brigatti et al., 2006). About 90% of a clay mineral's surface consists of nanometric interlayer spaces accessible to water molecules and other compounds. Clay minerals are swelling hydrated minerals (Borrego-Sánchez and Sainz-Díaz, 2022; Chen et al., 2022), thus the presence of clay could explain the observed high intensities of H and O detected in the filament compared to gypsum (Figure 8). This explains the presence of the

remaining elements at lower intensities, which are likely integrated into the composition or adsorbed (Figure 7A). The correlation is strongly supported by the absence or the significant decrease of most trace elements and biologically relevant chemical species in a clay-poor location, where only small Si and Al intensities are detected (Figure 7B).

Based on the structure, texture, and form of the clay minerals observed under SEM (Figures 4G,H), the clay mineral is most likely montmorillonite (a member of the smectite group), that forms as microscopic crystal precipitating from aqueous solutions (Christidis, 2012). Similar characteristics of hollow fossil filaments with traces of dolomite, carbonates and clay minerals were found in Messinian PLG at various locations across the Mediterranean Basin (Panieri et al., 2008; Natalicchio et al., 2022). The non-uniform horizontal and vertical distributions of the constituent chemical species, as depicted in Figures 8, 9B, are explained by the physical and chemical properties of dolomite and clay minerals.

The fossil filament also contains biologically relevant elements, which are primarily sequestered, adsorbed, or incorporated within the clay mineral structure due to its high capacity for adsorbing surrounding elements and organic molecules. The mass spectrum of the filament, presented in Figure 7, shows the presence of 19 metallic and non-metallic elements that are either directly, indirectly, or distantly related to life. For some of these elements, 2D atomic fraction maps are shown in Figure 8, including the CHNOPS elements (^{14}N map is not presented because of the possible interference with the doubly charged ^{28}Si ion). The major cations Mg, Na, K and Ca are also detected (Figure 7). K cations are essential for many key cellular processes, including protein synthesis. The Na^+/K^+ transmembrane proton gradient plays a crucial role in energy generation and maintaining cellular integrity in bacteria when facing osmotic stress (Dibrova et al., 2015). Both Mg and Ca play crucial roles as cations for all prokaryotes, though Ca is less abundant in bacteria compared to Mg (Wackett et al., 2004). These elements are integral to various prokaryotic processes and the formation of biofilms (Wang et al., 2019). Chlorine is also identified in the mass spectrum of the filament at location 110 (Figure 7A). The anion Cl^- is essential for the survival of some marine bacteria, such as the halophilic bacterium *Halobacillus halophilus* (Roeßler and Müller, 2002), acting as a key factor in signal transduction, gene expression modulation, and protein synthesis (Sewald et al., 2007). Which may have played a vital role in the survival of extremophiles during the MSC, when salinity levels rose to 130‰–160‰ (Warren, 2016).

Some transition metals including V, Mn, and Co were detected in the fossil filament. Some of these elements are essential for growth and survival, acting as growth-limiting factors for prokaryotes even at relatively low concentrations (Andreini et al., 2008; Bradley et al., 2020; Buccella et al., 2019). Cobalt, for instance, is deemed essential in more than 20 cobalamin-dependent enzymes in prokaryotes (Xiu et al., 2021). Vanadium is involved in respiration, central metabolism, and DNA repair (Frawley and Fang, 2014; Argüello et al., 2013; Rehder, 2015). Mn plays a critical role in protecting bacteria from cellular damage induced by various stressors, including UV-C radiation, gamma-irradiation, wet and dry heat, as well as hydrogen peroxide (H_2O_2). In the deposition environment of the PLG, these elements would have been vital for the living extremophile prokaryotes. Chromium was also detected; however, it is considered toxic, and some prokaryotes employ survival strategies such as adsorption, absorption, accumulation, and transformation within their cells (Zahoor and Rehman, 2009). In contrast, Ti's biological essentiality has not been discovered yet, although some marine bacteria have been observed adhering to TiO_2 particles (Hurst, 2022), which may be beneficial as a shield from UV radiations (Remick and Helmann, 2023).

The presence of Si detected in the fossil filament layers can be attributed to extracellular and intracellular bio-silicification by prokaryotes (Ikeda, 2021; Moore et al., 2020). This process allows cyanobacteria and other marine prokaryotes to survive harmful UV radiation by using siliceous deposits as a protective shield (Konhauser, 2006). It has also been demonstrated that silicon concentrations in some marine cyanobacteria are significantly higher than in sea water, suggesting an active silicon accumulation, often exceeding that of P and S (Ikeda, 2021). Considering the high salinity of the water column during the MSC–up to five times that of today's seawater (Warren, 2016) – the studied filament may have experienced both extracellular and intracellular Si accumulation (Baines et al., 2012). This accumulation may have caused cellular lysis during entombment within the gypsum matrix, indicated by the observed 10 μm long opening that connects the two holes, as shown in Figures 4G,H. It is also observed that the same mineralogical composition is observed in the two holes and at the opening connecting them, suggesting a mineral formation from the same primary solution, which might be the cell cytoplasm. The presence of gypsum only at the two sides of the opening, without effectively separating the holes, strongly indicates that the structural forces involved did not allow for an even distribution of the gypsum (Figure 4H).

Boron was also found to be essential for N fixation and growth under N-deficient conditions in some cyanobacteria (Miwa and Fujiwara, 2009). However, F, which was also detected within the fossil filament, primarily occurs as fluoride (F^-) in seawater and, along with certain transition metals, can be lethal to microorganisms when reaching certain concentrations (Pal et al., 2022). Lithium, despite its toxic nature, was also detected and is known to occur in certain marine bacteria living in salars (Remick and Helmann, 2023). The high-intensity peak of Al within the filament structure suggests its presence in the water column at elevated concentrations. However, Al lacks biological functionality and has low bioavailability. Its primary toxic effects in microbes arise from competition with Fe and Mg, as well as binding to DNA, membranes, or cell walls (Exley and Mold, 2015). Aluminum may have contributed to the formation of clay minerals through interaction with Si, O, and H. The presence of F, Al, and other toxic elements in the water column may have been responsible for cellular death, leading to the rapid entombment of filaments within the emerging PLG crystals.

4.2 Possible origin of dolomite and clay minerals

Dolomite is rare in modern sedimentary environments, although seawater is generally oversaturated with respect to dolomite (Gregg et al., 2015; Pina et al., 2022). Abiotic synthesis of

dolomite has been unsuccessful under Earth's surface conditions of 25°C and 1 bar (Braithwaite et al., 2004) and has only been achieved under specific conditions at temperatures of 95°C (Yang et al., 2022). In contrast, gypsum can be easily precipitated in laboratory experiments at ambient temperature (Disi et al., 2023). Furthermore, it was also proven that under diagenesis or metamorphic conditions (temperatures higher than 55°C) gypsum transforms into anhydrite (Engel et al., 2021). This transformation could rule out the possible abiotic formation of dolomite within gypsum, which requires high temperatures and pressure conditions (Yang et al., 2022).

The dolomitization reaction is endothermic and influenced by the Ca^{2+} and Mg^{2+} ratio. Moreover, water molecules reduce the availability of Mg^{2+} for dolomite crystal growth (Petrash et al., 2017). The synthesis of true stoichiometric dolomite without prokaryotes involvement at room temperature and pressure *in vitro* remains elusive (Yang et al., 2022; Pina et al., 2022; Han et al., 2022; Yasumoto-Hirose et al., 2022). During PLG crystallization, the elevated concentration of sulfates (SO_4^{2-}) does not inhibit dolomite formation (Sánchez-Román et al., 2009). Prokaryotes contribute to dolomite precipitation in two ways: (1) By increasing the surrounding alkalinity through various metabolic pathways and/or (2) Concentrating ions within the cell envelope and extracellular polymeric substances (EPS). This induces localized supersaturation of Ca^{2+} and Mg^{2+} ions, overcoming low-temperature kinetic barriers to dolomite formation (Sánchez-Román et al., 2008; Sánchez-Román et al., 2009; Chan et al., 2004; Fowle and Fein, 2001; Roberts et al., 2013; Moreira et al., 2004). This process could be applicable to sulfate reducing bacteria and in some environments to sulfide-oxidizing bacterial filaments thriving in the PLG depositional water column (Dela Pierre et al., 2015; Moreira et al., 2004).

Prokaryotes significantly contribute to clay mineral formation, primarily by supplying Fe, which interacts with dissolved Si and Al. Additionally, their EPS serve as nucleation sites for cation species, influencing mineral precipitation and cell encrustation (Joo et al., 2023; Konhauser, 2006; Konhauser and Urrutia, 1999; Alimova et al., 2009; Jaisi et al., 2007; Cuadros, 2017; Mueller, 2015). After cell death and during the mineral replacement process, the organic structure can act as a template and may preserve organic matter (Banfield et al., 2001). Furthermore, clay minerals promote bacterial biofilm formation by retaining water, as well as organic and inorganic nutrients, while also forming a mineral barrier shielding the biofilm from external environmental conditions (Cuadros, 2017). This explains the detection of clay minerals within the fossil filament layer associated with biologically relevant elements and organic inclusions.

4.3 Biogenicity and syngeneity of the fossil filament

Given the context of this study, determining the biogenicity and syngeneity of the filament is crucial for drawing meaningful conclusions about the discovery of biosignatures, especially in the context of Mars exploration. Several criteria have been proposed to assess the biogenicity of microbial fossils. These include evaluating the habitability of the paleoenvironment where the organism was fossilized, the presence of carbonaceous material, evidence of growth into a fluid-filled fracture, the non-uniformity of filament diameter, hollowness, sinuous and curved morphologies, Fe-oxide or clay composition, and semi-parallel growth of filament, (McMahon et al., 2020; McMahon et al., 2021; Oehler and Cady, 2014). These criteria align with the observations made in our study and those reported in other fossil bearing PLG across the Mediterranean Sea. Additionally, the observed alternations between turbid and limpid laminae in the studied PLG indicate periodic phases of microbial mat development and gypsum precipitation (Dela Pierre et al., 2012; Dela Pierre et al., 2014).

The paleontological and environmental context of the PLG and the studied fossil filament meets all the mentioned criteria, in addition to an observed potential indication of lysis within the filament. Moreover, the presence of dolomite and clay minerals serves as an indirect biosignature of life, as their formation is induced and/or influenced by prokaryotes (Cosmidis and Benzerara, 2022). Notably, the presence of an inner layer within the fossil filament strongly indicate that the filament was trapped during the primary crystallization of the PLG and is not a product of a secondary diagenesis of gypsum. Additionally, the general orientation of the fossil filaments, primarily parallel to the crystal growth plane, strongly suggest their syngenetic deposition as the PLG crystal grew.

4.4 Geomicrobiology of the Primary Lower Gypsum and implications for hydrated sulfates on Mars

The MSC was a brief yet impactful palaeoceanographic event that left a lasting imprint on the depositional environments of the Mediterranean. The sedimentary sequences linked to the MSC reflect rapid and profound environmental fluctuations, which challenged the adaptive capabilities of life forms in regions experiencing extreme conditions such as rapid evaporation, high salinity, anoxia, and desiccation leading to a notable dominance of halophilic archaea and bacteria. This shift is evidenced by the observed pattern in lipid biomarkers (Natalicchio et al., 2019), as well as variations in morphological and mineralogical diversity (Lugli et al., 2010; Natalicchio et al., 2013; Dela Pierre et al., 2015; Wang et al., 2023; Bailey et al., 2009). The presence of these biosignatures provides insights into the redox conditions at the seafloor and indicates an active biogeochemical sulfur cycle within Messinian brines (Schulz and Jørgensen, 2001). It is well documented that bacteria and archaea play a crucial role in the sulfur cycle during the crystallization of gypsum. This phenomenon has been observed at Gypsum Hill Spring in the Canadian High Arctic, where cold, hypersaline, anoxic conditions, and highly reducing brines rich in sulfate and sulfide characterize the environment. This environment serves as a Mars analog (Magnuson et al., 2023).

The shift in Martian climate from the wet Noachian era to the dry Hesperian period (4.1–3.0 billion years ago) likely led to the presence of saline surface waters rich in sulfur species (Macey et al., 2020b). As previously stated, this climatic transition resulted in the deposition of various sulfate minerals at different locations on Mars (Kounaves et al., 2010; Liu et al., 2024; Wilk et al., 2024; Rapin et al., 2019; Ettehadi et al., 2023). Recently, NASA's Perseverance rover

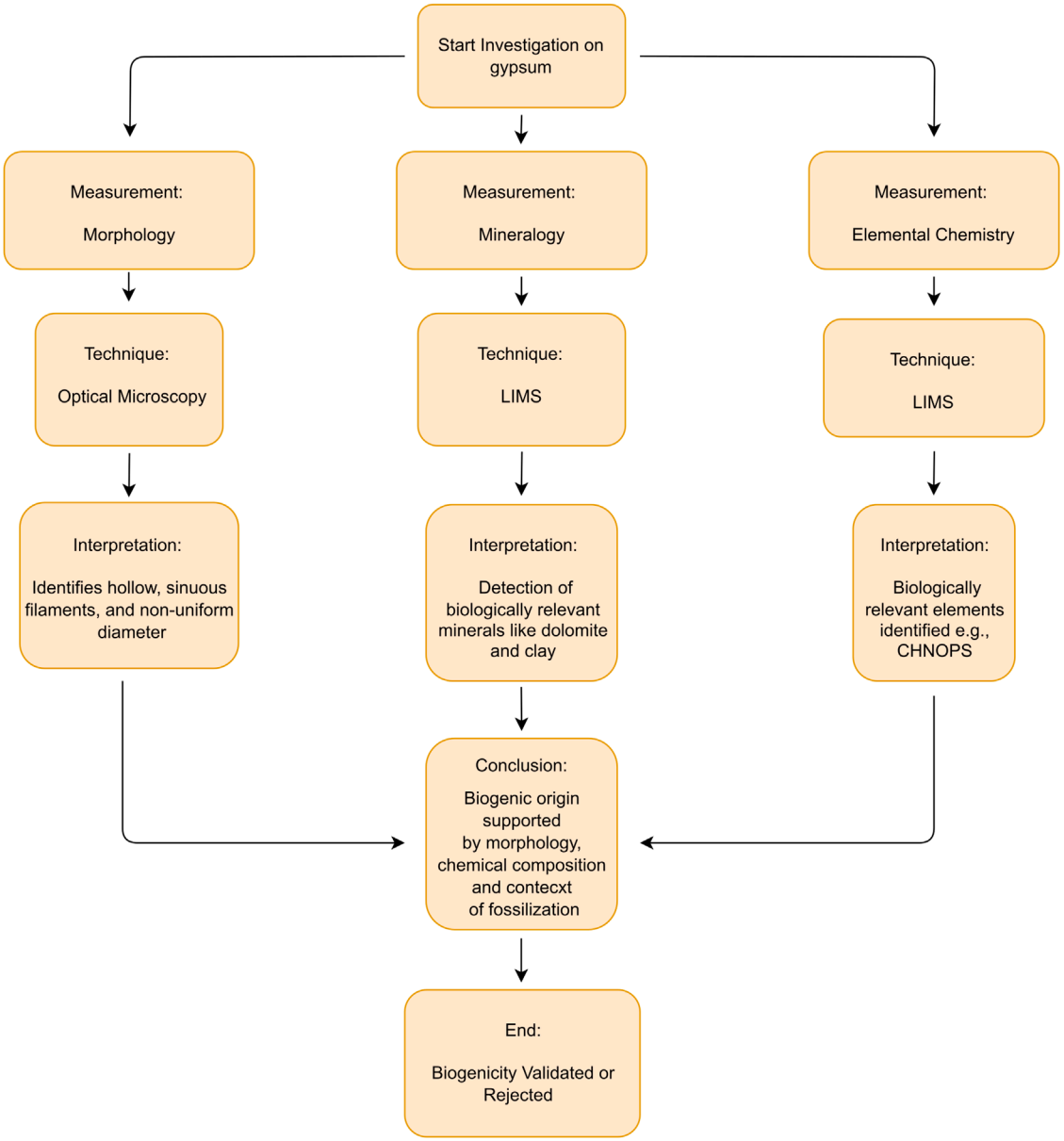

FIGURE 10
Flowchart for biosignatures detection in Martian gypsum.

has detected hydrated Ca-and Mg-sulfate minerals in the Noachian-age Jezero crater, which hosts a fan-delta system formed by a river draining into a paleolake. This lake was likely precipitated from a low temperature sulfate-rich fluid of moderate pH during multiple episodes (Siljeström et al., 2024).

The formation of hydrated gypsum on Mars suggests an origin in arid, oxidizing, saline, and acidic shallow surface groundwaters (Michalski et al., 2022; Benison and Bowen, 2006; Benison and LaClair, 2003; Squyres and Knoll, 2005). Given that, on Earth, the formation of carbonates (dolomite) depends on a thick atmosphere that moderates surface temperatures and a hydrosphere with a neutral to moderately alkaline nature (Fernández-Remolar et al., 2012), the occurrence of carbonate deposition on a cold and acidic Mars would have not been possible, conditions not favorable to maintain a relatively high activity of CO_3^{2-} anions in solution. In these low-pH depositional environments on Mars the abiotic origin of dolomite within gypsum could be ruled out and, prokaryotes, if ever existed, would have played a crucial role in forming dolomite by elevating overall alkalinity. Thus, if dolomite or carbonate minerals are discovered in Martian gypsum or hydrated sulfates in general, a prokaryotic origin should be considered.

It is important to emphasize that proto-dolomite formation may also be mediated by clay minerals, such as montmorillonite, at pH 9.7 (Liu et al., 2019). However, considering the acidic depositional environment associated with sulfate minerals on Mars, the potential mediation of protodolomite by montmorillonite is unlikely. Furthermore, given the low temperature and pressure

deposition conditions of ancient sulfate minerals on Mars, the abiotic formation of dolomites within gypsum, which requires high temperatures (95°C) and pressure conditions (Yang et al., 2022), could be ruled out. Also, if dolomite is formed abiotically under these high temperatures, the host gypsum containing dolomite, would have undergo diagenesis at earlier temperatures levels of 55°C and transforms to anhydrite (Engel et al., 2021). Despite this, the presence of dolomite should not be automatically interpreted as evidence of biological activity unless alternative origins can be conclusively ruled out (Banfield et al., 2001).

The presence of several other biosignatures detected with LIMS and optical microscopy in our study, which validate the biogenicity of the fossil filament, should be considered when searching for life in sulfate deposits on Mars. More intriguingly, the identification of clay minerals within the fossil filament has significant implications for investigating biosignatures on Mars. Firstly, the induced and influenced clay mineralization on the outer prokaryotic cells can serve as indirect evidence of biomineralization (Jaisi et al., 2007). Secondly, clay minerals demonstrate robust absorption capabilities, enhancing their potential for bio-preservation (Broz, 2020). Hence, it is highly probable that the clay minerals present significantly influenced the preservation of morphological and elemental biosignatures in the examined fossil filament and potentially in Martian hydrated sulfate minerals.

Figure 10 is a flowchart summarizing the complimentary measurements made in this study and, techniques used for each measurement, the interpretation that led to the conclusion about the biogenicity (or abiotic) origin of fossil filament.

5 Conclusion

This study highlights the potential of hydrated Messinian gypsum formed in a terrestrial analog to hydrated Martian sulfates to preserve bacterial biosignatures. To establish the biogenicity of potential biogenic structures, a comprehensive approach is required, encompassing the paleo-depositional context and atomic composition. The biogenicity and syngeneity of an Algerian PLG fossil filament were successfully established using a miniaturized space-prototype LIMS instrument in addition to optical microscopy. Complementary SEM and EDX measurements were performed to verify the presence of major elements.

LIMS proves to be a powerful analytical instrument for in-situ investigations of biosignatures, offering high spatial resolution and the capability to detect major and trace elements within fossil filaments. Using detailed chemical depth profiles and element maps, the composition of fossils can be accurately determined and distinguished from the host mineral (Wiesendanger et al., 2018; Lukmanov et al., 2021).

Although the MSC, during which the PLG formed, remains only partially understood, future astrobiological investigations on Mars should consider hydrated sulfate deposits as promising indicators of ancient Martian environmental conditions. This contribution underscores that hydrated sulfates serve as archives of biological history on Earth and potentially on Mars, should evidence of past life be found.

Data availability statement

The raw data supporting the conclusions of this article will be made available by the authors, without undue reservation.

Author contributions

YS: Conceptualization, Data curation, Formal Analysis, Investigation, Methodology, Project administration, Software, Writing–original draft, Writing–review and editing. SG: Data curation, Software, Writing–review and editing. MT: Conceptualization, Data curation, Investigation, Methodology, Project administration, Software, Supervision, Writing–review and editing. PK: Software, Writing–review and editing. AR: Methodology, Project administration, Supervision, Writing–review and editing. SM: Data curation, Writing–review and editing. PW: Conceptualization, Data curation, Funding acquisition, Investigation, Methodology, Project administration, Resources, Supervision, Validation, Writing–review and editing.

Funding

The author(s) declare that financial support was received for the research, authorship, and/or publication of this article. This work was supported by the financial support of Swiss National Science Foundation grant: 200020_207409. YS was supported by the ESKAS Swiss Government Excellence Scholarship 2022/24. This work has been carried out within the framework of the NCCR PlanetS supported by the Swiss National Science Foundation under grants 51NF40_182901 and 51NF40_205606.

Acknowledgments

YS would like to express his sincere gratitude to KNAUF Algeria in Oran for providing the studied material.

Conflict of interest

The authors declare that the research was conducted in the absence of any commercial or financial relationships that could be construed as a potential conflict of interest.

Generative AI statement

The authors declare that no Generative AI was used in the creation of this manuscript.

Publisher's note

All claims expressed in this article are solely those of the authors and do not necessarily represent those

of their affiliated organizations, or those of the publisher, the editors and the reviewers. Any product that may be evaluated in this article, or claim that may be made by its manufacturer, is not guaranteed or endorsed by the publisher.

Supplementary material

The Supplementary Material for this article can be found online at: https://www.frontiersin.org/articles/10.3389/fspas.2025.1503042/full#supplementary-material

References

Alimova, A., Katz, A., Steiner, N., Rudolph, E., Wei, H., Steiner, J. C., et al. (2009). Bacteria-Clay interaction: structural changes in smectite induced during biofilm formation. *Clays Clay Minerals* 57 (2), 205–212. doi:10.1346/ccmn.2009.0570207

Allwood, A., Burch, I. W., Rouchy, J. M., and Coleman, M. (2013b). Morphological biosignatures in gypsum: diverse formation processes of messinian (~6.0 ma) gypsum stromatolites. *Astrobiology* 13 (9), 870–886. doi:10.1089/ast.2013.1021

Anderson, D. E., Ehlmann, B. L., Forni, O., Clegg, S., Cousin, A., Thomas, N., et al. (2017). Characterization of LIBS emission lines for the identification of chlorides, carbonates, and sulfates in salt/basalt mixtures for the application to MSL ChemCam data. *J. Geophys. Res. Planets* 122 (4), 744–770. doi:10.1002/2016je005164

Andreini, C., Bertini, I., Cavallaro, G., Holliday, G. L., and Thornton, J. M. (2008). Metal ions in biological catalysis: from enzyme databases to general principles. *J. Biol. Inorg. Chem.* 13 (8), 1205–1218. doi:10.1007/s00775-008-0404-5

Argüello, J. M., Raimunda, D., and Padilla-Benavides, T. (2013). Mechanisms of copper homeostasis in bacteria. *Front. Cell. Infect. Microbiol.* 3, 73. doi:10.3389/fcimb.2013.00073

Bailey, J. V., Orphan, V. J., Joye, S. B., and Corsetti, F. A. (2009). Chemotrophic microbial mats and their potential for preservation in the rock record. *Astrobiology* 9 (9), 843–859. doi:10.1089/ast.2008.0314

Baines, S. B., Twining, B. S., Brzezinski, M. A., Krause, J. W., Vogt, S., Assael, D., et al. (2012). Significant silicon accumulation by marine picocyanobacteria. *Nat. Geosci.* 5 (12), 886–891. doi:10.1038/ngeo1641

Banfield, J. F., Moreau, J. W., Chan, C. S., Welch, S. A., and Little, B. J. (2001). Mineralogical biosignatures and the search for life on Mars. *Astrobiology* 1 (4), 447–465. doi:10.1089/153110701753593856

Barker, D. G., and Bhattacharya, J. P. (2018). Sequence stratigraphy on an early wet Mars. *Planet. Space Sci.* 151, 97–108. doi:10.1016/j.pss.2017.11.012

Baschetti, B., Frigeri, A., Altieri, F., Carli, C., Tullo, A., and Sgavetti, M. (2024). Paleoenvironmental significance of Fe/Mg phyllosilicate and sulfate deposits in Mikumi crater, northern Meridiani Planum, Mars. *Adv. Space Res.* 73, 2685–2702. doi:10.1016/j.asr.2023.12.060

Bellanca, A., Caruso, A., Ferruzza, G., Neri, R., Rouchy, J., Sprovieri, M., et al. (2001). Transition from marine to hypersaline conditions in the Messinian Tripoli Formation from the marginal areas of the central Sicilian Basin. *Sediment. Geol.* 140 (1–2), 87–105. doi:10.1016/s0037-0738(00)00173-1

Benison, K. C., and Bowen, B. B. (2006). Acid saline lake systems give clues about past environments and the search for life on Mars. *Icarus* 183 (1), 225–229. doi:10.1016/j.icarus.2006.02.018

Benison, K. C., and Karmanocky, F. J. (2014). Could microorganisms be preserved in Mars gypsum? Insights from terrestrial examples. *Geology* 42 (7), 615–618. doi:10.1130/g35542.1

Benison, K. C., and LaClair, D. A. (2003). Modern and ancient extremely acid saline deposits: terrestrial analogs for martian environments? *Astrobiology* 3 (3), 609–618. doi:10.1089/153110703322610690

Bibring, J., Langevin, Y., Gendrin, A., Gondet, B., Poulet, F., Berthé, M., et al. (2005). Mars surface diversity as revealed by the OMEGA/Mars Express observations. *Science* 307 (5715), 1576–1581. doi:10.1126/science.1108806

Borrego-Sánchez, A., and Sainz-Díaz, C. I. (2022). "Clay minerals as filters of drug compounds for green chemistry applications," in *Green chemistry and computational chemistry* (Elsevier eBooks), 403–423. doi:10.1016/b978-0-12-819879-7.00012-x

Bradley, J. M., Svistunenko, D. A., Wilson, M. T., Hemmings, A. M., Moore, G. R., and Brun, N. E. L. (2020). Bacterial iron detoxification at the molecular level. *J. Biol. Chem.* 295 (51), 17602–17623. doi:10.1074/jbc.rev120.007746

Braithwaite, C. J. R., Rizzi, G., and Darke, G. (2004). The geometry and petrogenesis of dolomite hydrocarbon reservoirs: introduction. *Geol. Soc. Lond. Spec. Publ.* 235 (1), 1–6. doi:10.1144/gsl.sp.2004.235.01.01

Brigatti, M. F., Galán, E., and Theng, B. K. G. (2006). "Chapter 2 structures and mineralogy of clay minerals," in *Developments in clay science*, 19–86. doi:10.1016/s1572-4352(05)01002-0

Broz, A. (2020). Organic matter preservation in ancient soils of Earth and Mars. *Life* 10 (7), 113. doi:10.3390/life10070113

Buccella, D., Lim, M. H., and Morrow, J. R. (2019). Metals in biology: from metallomics to trafficking. *Inorg. Chem.* 58 (20), 13505–13508. doi:10.1021/acs.inorgchem.9b02965

Carr, M. H., and Head, J. W. (2003). Oceans on Mars: an assessment of the observational evidence and possible fate. *J. Geophys. Res.* 108 (E5). doi:10.1029/2002je001963

Catling, D. C., Wood, S. E., Leovy, C. B., Montgomery, D. R., Greenberg, H., Glein, C. R., et al. (2006). Light-toned layered deposits in Juventae Chasma, Mars. *Icarus* 181 (1), 26–51. doi:10.1016/j.icarus.2005.10.020

Chan, M. A., Beitler, B., Parry, W., Ormö, J., and Komatsu, G. (2004). A possible terrestrial analogue for haematite concretions on Mars. *Nature* 429 (6993), 731–734. doi:10.1038/nature02600

Chen, W., Grabowski, R., and Goel, S. (2022). Clay swelling: role of cations in stabilizing/destabilizing mechanisms. *ACS Omega* 7 (4), 3185–3191. doi:10.1021/acsomega.1c04384

Christidis, G. E. (2012). "Industrial clays," in *EMU notes in mineralogy: vol. 9, chapter 9*, 341–414. doi:10.1180/emu-notes.9.9

Clark, B. C., Kolb, V. M., Steele, A., House, C. H., Lanza, N., Gasda, P. J., et al. (2021). Origin of life on Mars: suitability and opportunities. *Life* 11 (6), 539. doi:10.3390/life11060539

Clark, B. C., Morris, R. V., McLennan, S. M., Gellert, R., Jolliff, B. L., Knoll, A. H., et al. (2005). Chemistry and mineralogy of outcrops at Meridiani Planum. *Earth Planet. Sci. Lett.* 240 (1), 73–94. doi:10.1016/j.epsl.2005.09.040

Cloutis, E. A., Craig, M. A., Mustard, J. F., Kruzelecky, R. V., Jamroz, W. R., Scott, A., et al. (2007). Stability of hydrated minerals on Mars. *Geophys. Res. Lett.* 34 (20). doi:10.1029/2007gl031267

Cosmidis, J., and Benzerara, K. (2022). Why do microbes make minerals? *Comptes Rendus Géoscience* 354 (G1), 1–39. doi:10.5802/crgeos.107

Cuadros, J. (2017). Clay minerals interaction with microorganisms: a review. *Clay Miner.* 52 (2), 235–261. doi:10.1180/claymin.2017.052.2.05

Das, E., Mustard, J., Tarnas, J., Pascuzzo, A., and Kremer, C. (2021). Investigating the origin of gypsum in Olympia Undae: characterizing the mineralogy of the basal unit. *Icarus* 372, 114720. doi:10.1016/j.icarus.2021.114720

Dela Pierre, F., Clari, P., Bernardi, E., Natalicchio, M., Costa, E., Cavagna, S., et al. (2012). Messinian carbonate-rich beds of the Tertiary Piedmont Basin (NW Italy): microbially-mediated products straddling the onset of the salinity crisis. *Palaeogeogr. Palaeoclimatol. Palaeoecol.* 344–345, 78–93. doi:10.1016/j.palaeo.2012.05.022

Dela Pierre, F., Clari, P., Natalicchio, M., Ferrando, S., Giustetto, R., Lozar, F., et al. (2014). Flocculent layers and bacterial mats in the mudstone interbeds of the Primary Lower Gypsum unit (Tertiary Piedmont basin, NW Italy): archives of palaeoenvironmental changes during the Messinian salinity crisis. *Mar. Geol.* 355, 71–87. doi:10.1016/j.margeo.2014.05.010

Dela Pierre, F., Natalicchio, M., Ferrando, S., Giustetto, R., Birgel, D., Carnevale, G., et al. (2015). Are the large filamentous microfossils preserved in Messinian gypsum colorless sulfide-oxidizing bacteria? *Geology* 43 (10), 855–858. doi:10.1130/g37018.1

De Mol, M. L. (2023b). Astrobiology in Space: a Comprehensive look at the solar system. *Life* 13 (3), 675. doi:10.3390/life13030675

Dibrova, D. V., Galperin, M. Y., Koonin, E. V., and Mulkidjanian, A. Y. (2015). Ancient systems of sodium/potassium homeostasis as predecessors of membrane bioenergetics. *Biochem. Mosc.* 80 (5), 495–516. doi:10.1134/s0006297915050016

Disi, Z. A., Sadooni, F., Al-Kuwari, H. A., and Bontognali, T. R. R. (2023). Microbially influenced formation of anhydrite at low temperature. *Sci. Total Environ.* 902, 165820. doi:10.1016/j.scitotenv.2023.165820

Engel, M., Strohmenger, C. J., Peis, K. T., Pint, A., Brill, D., and Brückner, H. (2021). High-resolution facies analysis of a coastal sabkha in the eastern Gulf of Salwa (Qatar): a spatio-temporal reconstruction. *Sedimentology* 69 (3), 1119–1150. doi:10.1111/sed.12938

Enya, K., Yoshimura, Y., Kobayashi, K., and Yamagishi, A. (2022b). Extraterrestrial Life Signature Detection Microscopy: search and analysis of cells and organics on Mars and other solar system bodies. *Space Sci. Rev.* 218 (6), 49. doi:10.1007/s11214-022-00920-4

Ettehadi, A., Mokhtari, M., Chuprin, M., Anderson, R. C., Altun, G., and Heydari, E. (2023). Mechanical properties of terrestrial analogs to calcium sulfate veins on Gale crater, Mars. *Icarus* 406, 115760. doi:10.1016/j.icarus.2023.115760

Exley, C., and Mold, M. (2015). The binding, transport and fate of aluminium in biological cells. *J. Trace Elem. Med. Biol.* 30, 90–95. doi:10.1016/j.jtemb.2014.11.002

Fang, Y., Zhang, F., Farfán, G., and Xu, H. (2021). Low-Temperature synthesis of Disordered dolomite and High-Magnesium calcite in Ethanol–Water Solutions: the solvation effect and implications. *ACS Omega* 7 (1), 281–292. doi:10.1021/acsomega.1c04624

Fei, J., Shen, L., Guan, X., and Sun, Z. (2022). S and SR isotope compositions and trace element compositions of the Middle Jurassic evaporites in Eastern Tibet: provenance and palaeogeographic implications. *Minerals* 12 (8), 1039. doi:10.3390/min12081039

Fernández-Remolar, D. C., Morris, R. V., Gruener, J. E., Amils, R., and Knoll, A. H. (2005). The Río Tinto Basin, Spain: mineralogy, sedimentary geobiology, and implications for interpretation of outcrop rocks at Meridiani Planum, Mars. *Earth Planet. Sci. Lett.* 240 (1), 149–167. doi:10.1016/j.epsl.2005.09.043

Fernández-Remolar, D. C., Preston, L. J., Sánchez-Román, M., Izawa, M. R., Huang, L., Southam, G., et al. (2012). Carbonate precipitation under bulk acidic conditions as a potential biosignature for searching life on Mars. *Earth Planet. Sci. Lett.* 351 (352), 13–26. doi:10.1016/j.epsl.2012.07.015

Fowle, D. A., and Fein, J. B. (2001). Quantifying the effects of Bacillus subtilis cell walls on the precipitation of copper hydroxide from aqueous solution. *Geomicrobiol. J.* 18 (1), 77–91. doi:10.1080/01490450151079815

Frawley, E. R., and Fang, F. C. (2014). The ins and outs of bacterial iron metabolism. *Mol. Microbiol.* 93 (4), 609–616. doi:10.1111/mmi.12709

Gaboyer, F., Milbeau, C. L., Bohmeier, M., Schwendner, P., Vannier, P., Beblo-Vranesevic, K., et al. (2017). Mineralization and preservation of an extremotolerant bacterium isolated from an early Mars analog environment. *Sci. Rep.* 7 (1), 8775. doi:10.1038/s41598-017-08929-4

Gendrin, A., Mangold, N., Bibring, J., Langevin, Y., Gondet, B., Poulet, F., et al. (2005). Sulfates in martian layered terrains: the OMEGA/Mars express view. *Science* 307 (5715), 1587–1591. doi:10.1126/science.1109087

Gregg, J. M., Bish, D. L., Kaczmarek, S. E., and Machel, H. G. (2015). Mineralogy, nucleation and growth of dolomite in the laboratory and sedimentary environment: a review. *Sedimentology* 62 (6), 1749–1769. doi:10.1111/sed.12202

Grimaudo, V., Tulej, M., Riedo, A., Lukmanov, R., Ligterink, N. F. W., De Koning, C., et al. (2020). UV post-ionization laser ablation ionization mass spectrometry for improved nm-depth profiling resolution on Cr/Ni reference standard. *Rapid Commun. Mass Spectrom.* 34 (14), e8803. doi:10.1002/rcm.8803

Grotzinger, J. P., Sumner, D. Y., Kah, L. C., Stack, K., Gupta, S., Edgar, L., et al. (2013). A habitable fluvio-lacustrine environment at yellowknife bay, Gale crater, Mars. *Science* 343 (6169), 1242777. doi:10.1126/science.1242777

Gruchola, S., De Koning, C., Wiesendanger, R., Schmidt, P. K., Riedo, A., Grimaudo, V., et al. (2022). Improved limit of detection of a high-resolution fs-LIMS instrument through mass-selective beam blanking. *Int. J. Mass Spectrom.* 474, 116803. doi:10.1016/j.ijms.2022.116803

Guibourdenche, L., Cartigny, P., Dela Pierre, F., Natalicchio, M., and Aloisi, G. (2022). Cryptic sulfur cycling during the formation of giant gypsum deposits. *Earth Planet. Sci. Lett.* 593, 117676. doi:10.1016/j.epsl.2022.117676

Han, Z., Qi, P., Zhao, Y., Guo, N., Yan, H., Tucker, M. E., et al. (2022). High Mg/Ca molar ratios promote protodolomite precipitation induced by the extreme halophilic bacterium Vibrio harveyi QPL2. *Front. Microbiol.* 13, 821968. doi:10.3389/fmicb.2022.821968

Hazen, R. M., Downs, R. T., Morrison, S. M., Tutolo, B. M., Blake, D. F., Bristow, T. F., et al. (2023). On the diversity and formation modes of martian minerals. *J. Geophys. Res. Planets* 128 (9). doi:10.1029/2023je007865

Hsü, K. J., Ryan, W. B. F., and Cita, M. B. (1973). Late miocene desiccation of the Mediterranean. *Nature* 242 (5395), 240–244. doi:10.1038/242240a0

Huang, W., Ertekin, E., Wang, T., Cruz, L., Dailey, M., DiRuggiero, J., et al. (2020). Mechanism of water extraction from gypsum rock by desert colonizing microorganisms. *Proc. Natl. Acad. Sci. U. S. A.* 117 (20), 10681–10687. doi:10.1073/pnas.2001613117

Hurst, C. J. (2022). "Microbial metabolism of metals and metalloids," in *Advances in environmental microbiology*. doi:10.1007/978-3-030-97185-4

Ikeda, T. (2021). Bacterial biosilicification: a new insight into the global silicon cycle. *Biosci. Biotechnol. Biochem.* 85 (6), 1324–1331. doi:10.1093/bbb/zbab069

Jaisi, D. P., Dong, H., Kim, J., He, Z., and Morton, J. P. (2007). Nontronite particle aggregation induced by microbial Fe(III) reduction and exopolysaccharide production. *Clays Clay Minerals* 55 (1), 96–107. doi:10.1346/ccmn.2007.0550108

Joo, H., Kwon, T., and Dai, S. (2023). Clay-bacteria interaction: effect of bacterial cell density on sedimentation behavior and fabric map of kaolinite clay. *Appl. Clay Sci.* 241, 106973. doi:10.1016/j.clay.2023.106973

Kabiraj, A., Biswas, R., Halder, U., and Bandopadhyay, R. (2022). Bacterial arsenic metabolism and its role in arsenic bioremediation. *Curr. Microbiol.* 79 (5), 131. doi:10.1007/s00284-022-02810-y

King, P. L., and McLennan, S. M. (2010). Sulfur on Mars. *Elements* 6 (2), 107–112. doi:10.2113/gselements.6.2.107

Konhauser, K. O. (2006). *Introduction to geomicrobiology*. John Wiley and Sons.

Konhauser, K. O., and Urrutia, M. M. (1999). Bacterial clay authigenesis: a common biogeochemical process. *Chem. Geol.* 161 (4), 399–413. doi:10.1016/s0009-2541(99)00118-7

Kounaves, S. P., Hecht, M. H., Kapit, J., Quinn, R. C., Catling, D. C., Clark, B. C., et al. (2010). Soluble sulfate in the martian soil at the Phoenix landing site. *Geophys. Res. Lett.* 37 (9). n/a. doi:10.1029/2010gl042613

Krijgsman, W., Hilgen, F., Raffi, I., Sierro, F. J., and Wilsonk, D. (1991). Chronology, causes and progression of the Messinian salinity crisis. *Nature* 400 (6745), 652–655. doi:10.1038/23231

Krijgsman, W., Rohling, E. J., Palcu, D. V., Raad, F., Amarathunga, U., Flecker, R., et al. (2024). Causes and consequences of the Messinian salinity crisis. *Nat. Rev. Earth Environ.* 5 (5), 335–350. doi:10.1038/s43017-024-00533-1

Langevin, Y., Poulet, F., Bibring, J., and Gondet, B. (2005). Sulfates in the north polar region of Mars detected by OMEGA/Mars Express. *Science* 307 (5715), 1584–1586. doi:10.1126/science.1109091

Liu, D., Xu, Y., Papineau, D., Yu, N., Fan, Q., Qiu, X., et al. (2019). Experimental evidence for abiotic formation of low-temperature proto-dolomite facilitated by clay minerals. *Geochimica Cosmochimica Acta* 247, 83–95. doi:10.1016/j.gca.2018.12.036

Liu, J., Michalski, J., Gao, W., Schröder, C., and Li, Y. (2024). Freeze-thaw cycles drove chemical weathering and enriched sulfates in the Burns formation at Meridiani, Mars. *Sci. Adv.* 10 (3), eadi1805. doi:10.1126/sciadv.adi1805

Lugli, S., Manzi, V., Roveri, M., and Charlotte, S. B. (2010). The Primary Lower Gypsum in the Mediterranean: a new facies interpretation for the first stage of the Messinian salinity crisis. *Palaeogeogr. Palaeoclimatol. Palaeoecol.* 297 (1), 83–99. doi:10.1016/j.palaeo.2010.07.017

Lukmanov, R. A., De Koning, C., Schmidt, P. K., Wacey, D., Ligterink, N. F. W., Gruchola, S., et al. (2022). High mass resolution FS-LIMS imaging and manifold learning reveal insight into chemical diversity of the 1.88 GA Gunflint Chert. *Front. Space Technol.* 3. doi:10.3389/frspt.2022.718943

Lukmanov, R. A., Tulej, M., Ligterink, N. F. W., De Koning, C., Riedo, A., Grimaudo, V., et al. (2021). Chemical identification of microfossils from the 1.88-Ga Gunflint chert: towards empirical biosignatures using laser ablation ionization mass spectrometer. *J. Chemom.* 35 (10). doi:10.1002/cem.3370

Macey, M. C., Fox-Powell, M., Ramkissoon, N. K., Stephens, B., Barton, T., Schwenzer, S. P., et al. (2020b). The identification of sulfide oxidation as a potential metabolism driving primary production on late Noachian Mars. *Sci. Rep.* 10 (1), 10941. doi:10.1038/s41598-020-67815-8

Magnuson, E., Altshuler, I., Freyria, N. J., Leveille, R. J., and Whyte, L. G. (2023). Sulfur-cycling chemolithoautotrophic microbial community dominates a cold, anoxic, hypersaline Arctic spring. *Microbiome* 11 (1), 203. doi:10.1186/s40168-023-01628-5

Manzi, V., Gennari, R., Lugli, S., Roveri, M., Scafetta, N., and Schreiber, B. C. (2012). High-frequency cyclicity in the mediterranean messinian evaporites: evidence for solar-lunar climate forcing. *J. Sediment. Res.* 82 (12), 991–1005. doi:10.2110/jsr.2012.81

Massé, M., Bourgeois, O., Mouélic, S. L., Verpoorter, C., Spiga, A., and Deit, L. L. (2011). Wide distribution and glacial origin of polar gypsum on Mars. *Earth Planet. Sci. Lett.* 317–318, 44–55. doi:10.1016/j.epsl.2011.11.035

McMahon, S., Ivarsson, M., Wacey, D., Saunders, M., Belivanova, V., Muirhead, D., et al. (2021). Dubiofossils from a Mars-analogue subsurface palaeoenvironment: the limits of biogenicity criteria. *Geobiology* 19 (5), 473–488. doi:10.1111/gbi.12445

McMahon, S., Parnell, J., and Reekie, P. (2020). Mars-Analog Calcium sulfate veins Record evidence of ancient subsurface life. *Astrobiology* 20 (10), 1212–1223. doi:10.1089/ast.2019.2172

Michalski, J., Goudge, T. A., Crowe, S. A., Cuadros, J., Mustard, J. F., and Johnson, S. S. (2022). Geological diversity and microbiological potential of lakes on Mars. *Nat. Astron.* 6 (10), 1133–1141. doi:10.1038/s41550-022-01743-7

Miwa, H., and Fujiwara, T. (2009). Isolation and identification of boron-accumulating bacteria from contaminated soils and active sludge. *Soil Sci. Plant Nutr.* 55 (5), 643–646. doi:10.1111/j.1747-0765.2009.00402.x

Moore, K., Pajusalu, M., Gong, J., Sojo, V., Matreux, T., Braun, D., et al. (2020). Biologically mediated silicification of marine cyanobacteria and implications for the Proterozoic fossil record. *Geology* 48 (9), 862–866. doi:10.1130/g47394.1

Moreira, N., Walter, L. M., Vásconcelos, C., McKenzie, J. A., and McCall, P. J. (2004). Role of sulfide oxidation in dolomitization: sediment and pore-water geochemistry of a modern hypersaline lagoon system. *Geology* 32 (8), 701. doi:10.1130/g20353.1

Mueller, B. (2015). Experimental Interactions between clay minerals and Bacteria: a review. *Pedosphere* 25 (6), 799–810. doi:10.1016/s1002-0160(15)30061-8

Natalicchio, M., Birgel, D., Dela Pierre, F., Ziegenbalg, S. B., Hoffmann-Sell, L., Gier, S., et al. (2022). Messinian bottom-grown selenitic gypsum: an archive of microbial life. *Geobiology* 20 (1), 3–21. doi:10.1111/gbi.12464

Natalicchio, M., Dela Pierre, F., Birgel, D., Brumsack, H., Carnevale, G., Gennari, R., et al. (2019). Paleoenvironmental change in a precession-paced succession across the onset of the Messinian salinity crisis: insight from element geochemistry and molecular fossils. *Palaeogeogr. Palaeoclimatol. Palaeoecol.* 518, 45–61. doi:10.1016/j.palaeo.2019.01.009

Natalicchio, M., Dela Pierre, F., Clari, P., Birgel, D., Cavagna, S., Martire, L., et al. (2013). Hydrocarbon seepage during the messinian salinity crisis in the tertiary piedmont basin (NW Italy). *Palaeogeogr. Palaeoclimatol. Palaeoecol.* 390, 68–80. doi:10.1016/j.palaeo.2012.11.015

Neuland, M. B., Grimaudo, V., Mezger, K., Moreno-García, P., Riedo, A., Tulej, M., et al. (2016). Quantitative measurement of the chemical composition of geological standards with a miniature laser ablation/ionization mass spectrometer designed forin situapplication in space research. *Meas. Sci. Technol.* 27 (3), 035904. doi:10.1088/0957-0233/27/3/035904

Oehler, D. Z., and Cady, S. L. (2014). Biogenicity and syngeneity of organic matter in ancient sedimentary rocks: recent advances in the search for evidence of past life. *Challenges* 5 (2), 260–283. doi:10.3390/challe5020260

Oliveri, E., Neri, R., Bellanca, A., and Riding, R. (2009). Carbonate stromatolites from a Messinian hypersaline setting in the Caltanissetta Basin, Sicily: petrographic evidence of microbial activity and related stable isotope and rare earth element signatures. *Sedimentology* 57 (1), 142–161. doi:10.1111/j.1365-3091.2009.01094.x

Pal, K. C., Mukhopadhyay, P., Chatterjee, S., and Mondal, N. K. (2022). A study on fluoride bioremediation via a novel bacterium Bacillus megaterium (JF273850) isolated from agricultural soil. *J. Earth Syst. Sci.* 131 (3), 183. doi:10.1007/s12040-022-01931-z

Panieri, G., Lugli, S., Manzi, V., Palinska, K. A., and Roveri, M. (2008). Microbial communities in Messinian evaporite deposits of the Vena del Gesso (northern Apennines, Italy). *Stratigraphy* 5 (3–4), 343–352. doi:10.29041/strat.05.3.09

Panieri, G., Lugli, S., Manzi, V., Roveri, M., Schreiber, B. C., and Palińska, K. A. (2010). Ribosomal RNA gene fragments from fossilized cyanobacteria identified in primary gypsum from the late Miocene, Italy. *Geobiology* 8 (2), 101–111. doi:10.1111/j.1472-4669.2009.00230.x

Pellegrino, L., Natalicchio, M., Abe, K., Jordan, R. W., Longo, S. E. F., Ferrando, S., et al. (2021). Tiny, glassy, and rapidly trapped: the nano-sized planktic diatoms in Messinian (late Miocene) gypsum. *Geology* 49 (11), 1369–1374. doi:10.1130/g49342.1

Perri, E., Gindre-Chanu, L., Caruso, A., Cefalà, M., Scopelliti, G., and Tucker, M. E. (2017). Microbial-mediated pre-salt carbonate deposition during the Messinian salinity crisis (Calcare di Base fm., Southern Italy). *Mar. Petroleum Geol.* 88, 235–250. doi:10.1016/j.marpetgeo.2017.08.028

Petrash, D. A., Bialik, O. M., Bontognali, T. R. R., Vásconcelos, C., Roberts, J. a. F., McKenzie, J. A., et al. (2017). Microbially catalyzed dolomite formation: from near-surface to burial. *Earth-Science Rev.* 171, 558–582. doi:10.1016/j.earscirev.2017.06.015

Pina, C. M., Pimentel, C., and García-Crespo, Á. (2022). The dolomite problem: a matter of time. *ACS Earth Space Chem.* 6 (6), 1468–1471. doi:10.1021/acsearthspacechem.2c00078

Rapin, W., Ehlmann, B. L., Dromart, G., Schieber, J., Thomas, N., Fischer, W. W., et al. (2019). An interval of high salinity in ancient Gale crater lake on Mars. *Nat. Geosci.* 12 (11), 889–895. doi:10.1038/s41561-019-0458-8

Rehder, D. (2015). The role of vanadium in biology. *Metallomics* 7 (5), 730–742. doi:10.1039/c4mt00304g

Remick, K. A., and Helmann, J. D. (2023). The elements of life: a biocentric tour of the periodic table. *Adv. Microb. Physiology* 82, 1–127. doi:10.1016/bs.ampbs.2022.11.001

Riedo, A., Lukmanov, R., Grimaudo, V., De Koning, C., Ligterink, N. F. W., Tulej, M., et al. (2021). Improved plasma stoichiometry recorded by laser ablation ionization mass spectrometry using a double-pulse femtosecond laser ablation ion source. *Rapid Commun. Mass Spectrom.* 35 (12), e9094. doi:10.1002/rcm.9094

Riedo, A., Tulej, M., Rohner, U., and Würz, P. (2017). High-speed microstrip multi-anode multichannel plate detector system. *Rev. Sci. Instrum.* 88 (4), 045114. doi:10.1063/1.4981813

Roberts, J. a. F., Kenward, P. A., Fowle, D. A., Goldstein, R. H., González, L. A., and Moore, D. S. (2013). Surface chemistry allows for abiotic precipitation of dolomite at low temperature. *Proc. Natl. Acad. Sci. U. S. A.* 110 (36), 14540–14545. doi:10.1073/pnas.1305403110

Roeβler, M., and Müller, V. (2002). Chloride, a new environmental signal molecule involved in gene regulation in a moderately halophilic bacterium, Halobacillus halophilus. *J. Bacteriol.* 184 (22), 6207–6215. doi:10.1128/jb.184.22.6207-6215.2002

Rouchy, J. M., Caruso, A., Cartigny, P., Blanc-Valleron, M., and Bassetti, M. A. (2007). The end of the messinian salinity crisis: evidence from the Chelif Basin (Algeria). *Palaeogeogr. Palaeoclimatol. Palaeoecol.* 254 (3–4), 386–417. doi:10.1016/j.palaeo.2007.06.015

Roveri, M., Flecker, R., Krijgsman, W., Lofi, J., Lugli, S., Manzi, V., et al. (2014). The Messinian Salinity Crisis: past and future of a great challenge for marine sciences. *Mar. Geol.* 352, 25–58. doi:10.1016/j.margeo.2014.02.002

Sajjad, W., Ilahi, N., Ghimire, P. S., Bahadur, A., Zada, S., and Iqbal, A. (2022). Endolithic microbes of rocks, their community, function and survival strategies. *Int. Biodeterior. Biodegrad.* 169, 105387. doi:10.1016/j.ibiod.2022.105387

Sánchez-Román, M., McKenzie, J. A., De Luca Rebello Wagener, Â., Rivadeneyra, M. A., and Vásconcelos, C. (2009). Presence of sulfate does not inhibit low-temperature dolomite precipitation. *Earth Planet. Sci. Lett.* 285 (1–2), 131–139. doi:10.1016/j.epsl.2009.06.003

Sánchez-Román, M., Vásconcelos, C., Schmid, T. W., Dittrich, M., McKenzie, J. A., Zenobi, R., et al. (2008). Aerobic microbial dolomite at the nanometer scale: implications for the geologic record. *Geology* 36 (11), 879. doi:10.1130/g25013a.1

Schopf, J. W., Farmer, J. D., Foster, I., Kudryavtsev, A. B., Gallardo, V. A., and Espinoza, C. (2012). Gypsum-Permineralized microfossils and their relevance to the search for life on Mars. *Astrobiology* 12 (7), 619–633. doi:10.1089/ast.2012.0827

Schulz, H. N., and Jørgensen, B. B. (2001). Big bacteria. *Annu. Rev. Microbiol.* 55 (1), 105–137. doi:10.1146/annurev.micro.55.1.105

Sefton-Nash, E., Catling, D., Wood, S., Grindrod, P., and Teanby, N. (2012). Topographic, spectral and thermal inertia analysis of interior layered deposits in Iani Chaos, Mars. *Icarus* 221 (1), 20–42. doi:10.1016/j.icarus.2012.06.036

Sewald, X., Saum, S. H., Palm, P., Pfeiffer, F., Oesterhelt, D., and Müller, V. (2007). Autoinducer-2-Producing protein LuxS, a novel salt- and chloride-induced protein in the moderately halophilic bacterium Halobacillus halophilus. *Appl. Environ. Microbiol.* 73 (2), 371–379. doi:10.1128/aem.01625-06

Sgavetti, M., Pompilio, L., Roveri, M., Manzi, V., Valentino, G., Lugli, S., et al. (2009b). Two geologic systems providing terrestrial analogues for the exploration of sulfate deposits on Mars: initial spectral characterization. *Planet. Space Sci.* 57 (5–6), 614–627. doi:10.1016/j.pss.2008.05.010

Siljeström, S., Czaja, A. D., Corpolongo, A., Berger, E. L., Li, A. Y., Cardarelli, E., et al. (2024). Evidence of sulfate-rich fluid alteration in Jezero crater floor, Mars. *J. Geophys. Res. Planets* 129 (1). doi:10.1029/2023je007989

Squyres, S. W., Arvidson, R. E., Bell, J. F., Calef, F., Clark, B. C., Cohen, B. A., et al. (2012). Ancient impact and aqueous processes at Endeavour Crater, Mars. *Science* 336 (6081), 570–576. doi:10.1126/science.1220476

Squyres, S. W., and Knoll, A. H. (2005). Sedimentary rocks at Meridiani Planum: origin, diagenesis, and implications for life on Mars. *Earth Planet. Sci. Lett.* 240 (1), 1–10. doi:10.1016/j.epsl.2005.09.038

Tang, Y., Gao, J., Liu, C., Chen, X., and Zhao, Y. (2019). Dehydration pathways of gypsum and the rehydration mechanism of soluble anhydrite Γ-CASO4. *ACS Omega* 4 (4), 7636–7642. doi:10.1021/acsomega.8b03476

Teske, A., and Nelson, D. C. (2006). *The genera Beggiatoa and Thioploca*. Springer eBooks, 784–810. doi:10.1007/0-387-30746-x_27

Tulej, M., Wiesendanger, R., Riedo, A., Knopp, G., and Wurz, P. (2018). Mass spectrometric analysis of the Mg plasma produced by double-pulse femtosecond laser irradiation. *J. Anal. Atomic Spectrom.* 33 (8), 1292–1303. doi:10.1039/c8ja00036k

Vai, G. B., and Lucchi, F. (1977). Algal crusts, autochthonous and clastic gypsum in a cannibalistic evaporite basin: a case history from the Messinian of Northern Apennines. *Sedimentology* 24 (2), 211–244. doi:10.1111/j.1365-3091.1977.tb00255.x

Vaniman, D. T., Martínez, G., Rampe, E. B., Bristow, T. F., Blake, D. F., Yen, A. S., et al. (2018). Gypsum, bassanite, and anhydrite at Gale crater, Mars. *Am. Mineralogist* 103 (7), 1011–1020. doi:10.2138/am-2018-6346

Wackett, L. P., Dodge, A. G., and Ellis, L. B. M. (2004). Microbial genomics and the periodic table. *Appl. Environ. Microbiol.* 70 (2), 647–655. doi:10.1128/aem.70.2.647-655.2004

Wang, T., Flint, S., and Palmer, J. W. (2019). Magnesium and calcium ions: roles in bacterial cell attachment and biofilm structure maturation. *Biofouling* 35 (9), 959–974. doi:10.1080/08927014.2019.1674811

Wang, T., Zhong, G., Liu, H., Liu, H., Xia, Y., and Xun, L. (2023). A common mechanism for rapid transfer of zero-valent sulfur between microbial cells. *Sci. Total Environ.* 891, 164461. doi:10.1016/j.scitotenv.2023.164461

Warren, J. K. (2016). "Evaporites," in *Encyclopedia of Earth Sciences*, 1–8. doi:10.1007/978-3-319-39193-9_100-1

Westall, F., Foucher, F., Bost, N., Bertrand, M., Loizeau, D., Vago, J. L., et al. (2015). Biosignatures on Mars: what, where, and how? Implications for the search for Martian life. *Astrobiology* 15 (11), 998–1029. doi:10.1089/ast.2015.1374

Wiesendanger, R., Wacey, D., Tulej, M., Neubeck, A., Ivarsson, M., Grimaudo, V., et al. (2018). Chemical and optical identification of micrometer-sized 1.9-billion-year-old fossils by combining a miniature laser ablation ionization mass spectrometry system with an optical microscope. *Astrobiology* 18 (8), 1071–1080. doi:10.1089/ast.2017.1780

Wilk, K., Bishop, J. L., Weitz, C. M., Parente, M., Saranathan, A. M., Itoh, Y., et al. (2024). Characterization of aqueous alteration and formation of salty exposures at Ius Chasma, Mars. *Icarus* 408, 115800. doi:10.1016/j.icarus.2023.115800

Wray, J. J., Milliken, R. E., Dundas, C. M., Swayze, G. A., Andrews-Hanna, J. C., Baldridge, A. M., et al. (2011). Columbus crater and other possible groundwater-fed paleolakes of Terra Sirenum, Mars. *J. Geophys. Res. Atmos.* 116 (E1), E01001. doi:10.1029/2010je003694

Wray, J. J., Squyres, S. W., Roach, L. H., Bishop, J. L., Mustard, J. F., and Dobrea, E. Z. N. (2010). Identification of the Ca-sulfate bassanite in Mawrth Vallis, Mars. *Icarus* 209 (2), 416–421. doi:10.1016/j.icarus.2010.06.001

Xiu, H., Wei, X., Liu, J., and Chen, J. (2021). Cobalt: an essential micronutrient for plant growth? *Front. Plant Sci.* 12, 768523. doi:10.3389/fpls.2021.768523

Yang, L., Yu, L., Liu, K., Jia, J., Zhu, G., and Liu, Q. (2022). Coupled effects of temperature and solution compositions on metasomatic dolomitization: significance and implication for the formation mechanism of carbonate reservoir. *J. Hydrology* 604, 127199. doi:10.1016/j.jhydrol.2021.127199

Yasumoto-Hirose, M., Yasumoto, K., Iijima, M., Nishino, T., Ikemoto, E., Nishijima, M., et al. (2022). Mg-rich calcite-producing marine bacterium Pseudovibrio sp. isolated from an ascidian in coral reefs at Okinawa, Japan. *Fish. Sci.* 88 (5), 625–634. doi:10.1007/s12562-022-01627-9

Yoshimura, Y. (2019). *The search for life on Mars*. Springer eBooks, 367–381. doi:10.1007/978-981-13-3639-3_23

Zahoor, A., and Rehman, A. (2009). Isolation of Cr(VI) reducing bacteria from industrial effluents and their potential use in bioremediation of chromium containing wastewater. *J. Environ. Sci.* 21 (6), 814–820. doi:10.1016/s1001-0742(08)62346-3